DRAG REDUCTION BY POLYMERIC ADDITIVE SOLUTIONS

Jorge A. Clares Pastrana

Thesis submitted to the Faculty of the

Virginia Polytechnic Institute and State University

in partial fulfillment of the requirements for the degree of

Master of Science

in

Aerospace Engineering

Eric G. Paterson, Chair

Stefano Brizzolara

Christopher J. Roy

September 6, 2023

Blacksburg, Virginia

Keywords: Computational Fluid Dynamics, OpenFOAM, Drag Reduction, Polymer

DRAG REDUCTION BY POLYMERIC ADDITIVE SOLUTIONS

Jorge A. Clares Pastrana

(ABSTRACT)

Historically, the addition of polymers to turbulent flows of Newtonian fluids has been known to effectively reduce turbulent friction drag by up to 80 %. Conducted in the Hydrodynamics Laboratory in Virginia Tech, this research presents a comprehensive analysis into drag reducing effects through experimental, theoretical, and computational analyses. A major focus of this research was the evaluation of one of the newest viscoelastic Reynolds Averaged Navier-Stokes (RANS) turbulence models. Based on the $k-\varepsilon-v^2-f$ framework, this model describes the viscoelastic effects of polymer additives using the Finitely Extensible Nonlinear Elastic-Peterlin (FENEP) constitutive model. To evaluate its accuracy, multiple simulation scenarios were benchmarked against Direct Numerical Simulation (DNS) data. Results indicated, that the viscoelastic RANS turbulence model shows a high accuracy against DNS percentages of drag reduced when dealing with higher solvent viscosity to polymer viscosity ratios, but revealed inconsistencies at lower ratios. Additionally, our theoretical and empirical flow rates from the inclined channel were closely aligned. The results of this study highlight the significant capacity of polymer additives to improve energy efficiency in industries that heavily rely on fluids.

DRAG REDUCTION BY POLYMERIC ADDITIVE SOLUTIONS

Jorge A. Clares Pastrana

(GENERAL AUDIENCE ABSTRACT)

In fluid dynamics, understanding the behavior of fluids under different conditions can unlock solutions to many engineering challenges. An area of much interest is the introduction of polymers to turbulent flows. The addition of polymers to turbulent flows can effectively dampen turbulence, leading to reduced drag. Our research, conducted at Virginia Tech's Hydrodynamics Laboratory, engaged in further study regarding this phenomena. We employed one of the latest viscoelastic computational models to predict drag reduction in polymer additive flows. This advanced model operates on the foundation of certain mathematical constructs, taking into account various parameters associated with polymeric solutions. By comparing our model's predictions with high end direct numerical simulations (DNS), we found it to be highly accurate, especially when the base fluid had a much higher viscosity than the polymer additives. But, it's worth noting that the model showed some deviations in cases where this viscosity difference was less pronounced. Furthermore, our tests also showcased a close alignment between predicted and observed flow rates in an inclined channel setup. Our findings underscore the potential of polymers to revolutionize industries, enhancing energy efficiency in processes that involve fluid flows

Dedication

Arturo Clares Martinez & Irma Pastrana

Acknowledgments

I would like to give my profound appreciation to my mentor and advisor Dr. Eric Paterson for his guidance throughout my academic journey, and for all the knowledge, support and advice he shared with me. I would also like to thank my committee members Dr. Stefano Brizzolara and Dr. Christopher Roy for their knowledge, feedback and enthusiasm on my research and thesis.

I wish to express my sincere gratitude to my colleagues for their constant support and encouragement throughout this journey. I would also like to thank Dr. Tod Lowe and Dr. Pat Artis, for their invaluable insight and knowledge that helped me further my understanding of Aerospace Engineering.

My final appreciation goes to my Family. My Mother, Father and Sisters, for their relentless and indefatigable support throughout my entire life. They were, are, and always will be the driving force that motivates me to strive for excellence and overcome every challenge that comes my way.

Contents

List of Figures

List of Tables

List of Abbreviations

ϵ	Dissipation Rate
η_p	Polymer Intrinsic Viscosity
λ	Relaxation Time
ν_s	Viscosity of Solvent
ν_t	Turbulent Viscosity
$\nu_{t,p}$	Turbulent Polymer Viscosity
$\overline{\nu^2}$	Turbulent Kinetic Energy Wall Normal Component
ρ	density
C_{kk}	Trace of Conformation Tensor
L^2	Maximum Extension of the Polymer Chains
u_τ	Friction Velocity
U_i	Mean Velocity
u_i	Velocity Component
$We_{\tau o}$	Weissenberg Number
a_1	Model Constant
a_2	Model Constant

a_3	Model Constant
C	Concentration
C_f	Friction Coefficient
C_{ij}	Mean Conformation Tensor
CFD	Computational Fluid Dynamics
f	Darcy Friction Factor
f	Energy Redistribution Process
h	Height of Channel
p	Pressure
PDR	Polymer Drag Reduction
ppm	Parts per Million
u^+	Normalized Velocity
y	Normal Distance From The Wall
y^+	Normalized Distance From The Wall

Chapter 1

Introduction

For over 70 years, it has been known, that the addition of polymers to turbulent flows of Newtonian fluids can dramatically reduce the turbulent friction drag up to 80%. Extensive analyses of the early literature in this field are provided in Virk , Lumley and Hoyt. Several researchers have found considerable success in the field of numerical simulation of diluted polymer solutions. Viscoelastic models like Oldroyd-B and Finitely Extensible Nonlinear Elastic-Peterlin (FENE-P) are frequently used to explore these fluids. The FENE-P model is frequently used in literature because it takes chain extensibility into account White and Mungal. Understanding how rheological parameters affect turbulent structure and statistics has been the focus of several DNS research of fully-developed turbulent channel flow Dimitropoulos et al.. Direct Numerical Simulation (DNS) of turbulent viscoelastic flow is significantly more expensive than Newtonian DNS because of the larger number of primary variables in the former than in the latter Li et al.. Due to this high costs, several researchers Pinho, Pinho et al. and Iaccarino et al. have developed Reynolds Averaged Navier-Stokes (RANS) models based on the DNS results. Masoudian et al. proposed the latest viscoelastic RANS turbulence model based on the k - $\epsilon - v^2 - f$ turbulence model, in which they propose new precise closures for the nonlinear turbulent terms. Their results were in better agreement with DNS data proposed by Pinho et al.,Pinho et al. and Iaccarino et al..

The goal of this study is to deeply understand the fundamental principles of fluid dynamics, perform both theoretical and experimental analyses of the hydrodynamic laboratory in Virginia Tech, and to evaluate the viscoelastic RANS turbulence model developed by Masoudian et al. in predicting Drag Reduction (DR) values. As mentioned, this study takes a theoretical, experimental and Computational Fluid Dynamics (CFD) approach to analyze the benefits and limitations which polymer additives present. The significance of this topic is that polymer additives have the potential to significantly reduce energy consumption in fluid handling systems and thus have implications for industries where fluid flow is a critical part of the operational process.

1.1 Background & Motivation

Drag reduction has become a phenomenon of significant scientific and industrial interest. The act of reducing drag refers to the process by which the frictional drag within a flow system is minimized, resulting in improved efficiency and reduced energy consumption White and Majdalani. The resulting advantages of reducing the energy consumption of a system have propelled the exhaustive search for different ways to reduce drag. According to Kalelkar et al., one of the most promising techniques to achieve drag reduction is the use of polymers. This has resulted in a tireless effort to find the best possible attainable polymeric solution that minimizes the drag encountered. The emerge of CFD has revolutionized the approach taken to research and understand the problems that emerge from analyzing fluid flows. In a world where energy efficiency and environmental sustainability has become imperative, the importance of drag reducing techniques is important.

On a personal level, the motivation for this dissertation comes from a scientific perspective, but also from an environmental one. The scientific motivation behind this study is the potential to significantly enhance the understanding of the benefits that polymeric solutions represent in toady's world. The utilization of polymers could ultimately transform industries that rely on fluid flow systems. From an environmental perspective, the motivations for this study are represented by the strong aspirations for world preservation. The potential of contributing to energy efficiency efforts and helping to mitigate the environmental impact fuels this research. In conclusion, the motivations behind this dissertation are: to deepen the understanding of one of the most prominent drag reduction mechanisms, to exploit the potential of polymeric additive solutions, and to channel the capabilities of CFD to develop accurate representations of polymeric fluid flows.

1.2 Literature Review

There has been substantial research on the effects that polymer has when it comes to reducing drag. These studies span several decades and encompass a variety of disciplines. Since the 1940's, drag reduction has been a topic of intense interest in the scientific and industrial communities Agarwal et al.. The oil crisis of the era made imminent the need for energy efficiency, prompting researchers to explore various strategies to minimize drag in fluid flow systems. Among the techniques studied, the addition of high molecular weight polymers to the fluid stream was found to significantly decrease the frictional drag Virk. This discovery, building on the foundational work of Toms, led to countless amounts of research investigating the effects of different polymers, their optimal concentrations, and the mechanisms underlying their drag-reducing capabilities. Since then, studies have ranged from laboratory experiments to computational simulations, each contributing new insights and progressively refining our understanding of this complex phenomenon. Two primary theories emerged to explain drag reduction. Lumley attributed the phenomena to the stretching of the polymers, contending that this raised the effective viscosity, particularly in regions of severe deformation like the buffer layer. In turn, this dampened minor eddies, thickened the viscous sublayer, and decreased drag. De Gennes, claimed the opposite, claiming that the elastic rather than the viscous characteristics of polymers were what caused drag to be reduced. Experiments performed by McComb and Rabie, later proved that it was the elastic rather than the viscous characteristics of polymers what caused drag to be reduced.

1.2.1 Experimental Studies on Polymer Drag Reduction

Historically, Toms published data on the flow at large Reynolds numbers of polymeric solutions through straight tubes. He discovered that adding the polymer to a solvent could significantly boost flow rate while maintaining a consistent pressure gradient; this is known as turbulent-flow friction reduction. This has now become a focus of research, with other polymers and solvents being put through comparable tests. Van Der Meulen provides valuable comparative insights into four differnet types of polymers: Guar Gum, Separan NP-10, Polyox WSR-301, and CMC. All three, Guar Gum, Separan NP-10, and Polyox WSR-301 displayed nearly identical maximum friction reductions, while their effectiveness varied significantly. Specifically, Polyox WSR-301 emerged as the most effective, requiring far lesser concentration to achieve similar friction reduction as the others. In their study, Van Der Meulen made the important observation that the most effective polymers were also the most prone to degradation. Polyox WSR-301 and Separan NP-10, while highly effective in reducing friction, were found to be vulnerable to mechanical breakdown. Wu et al. focused on assessing drag reduction across varying ejection velocities and concentrations. The outcomes of their experiments shed light on several aspects of the problem. For instance, drag reduction efficiency, when considered in the context of varying polymer ejection concentrations, appears to align well with established semi-empirical models, particularly the Prandlt Schlichting law. Wu et al. makes an important observation of how the location of polymer ejection influenced drag reduction efficiency. He continues to observe in their study that while concentrations equal to or less than 500 Parts per Million (ppm) aligned well with the empirical diffusion model, concentrations exceeding 500 ppm saw a decline in efficiency. Staying in the topic of drag reduction by the injection of polymeric solutions, the research presented by Walker et al., observes that long-chain polymer molecules, when effectively situated in the wall region of a turbulent flow, lead to reduced viscous drag. Walker et al.

observed that the combination of slot angle and width were also important, drag reduction primarily depended on the injection concentration and flow rate. As stated above, Walker et al. concluded that the optimal performance was observed at an injection flow rate of 450 ml/min and a concentration of 700ppm. Finally, their study concluded that even low additive concentrations below 3 ppm resulted in a 30 % drag reduction, possibly due to the additives achieving a favorable structure for reducing drag by the time they reached the effective zones. Wu and Tulin

1.2.2 CFD in Polymer Drag Reduction

Direct Numerical Simulation:

Modern computational numerical simulations of turbulent flow with polymers have employed models that represent the polymers as Finitely Extensible Nonlinear Elastic (FENE) bead-spring chains. Studies by Sureshkumar et al. and Dimitropoulos et al., made use of the Finitely Extensible Nonlinear Elastic-Peterlin (FENE-P) model, a more thorough polymer model that offers a more precise depiction of the interactions between the polymer and flow. Their research made predictions about turbulence statistics and drag reduction that were in line with the results of experiments. Due to the high computational cost, high drag reduction regimes have not been extensively explored by numerical simulations. The work of Warholic et al. and Ptasinski et al., observed critical behaviors near the maximum drag reduction limit and how they significantly impact turbulence. More recently, turbulent channel flow has been directly numerically simulated (DNS) under circumstances close to the maximum drag reduction. By combining high Reynolds numbers, high polymer concentrations, and extremely extensible polymers, Ptasinski et al. was able to achieve these regimes. In their study, the most significant finding is the agreement that has been found between comparisons

with experimental data for many features of turbulent behavior, including the mean velocity profile and turbulence statistics.

When talking about computational numerical simulation with respect to polymer drag reduction, a significant part of the drag reduction literature discusses the role of the Weissenberg number ($We_{\tau 0}$) in turbulent flows with polymer additives. According to the study by Bird and Armstrong, the Weissenberg number represents the ratio of the characteristic time of fluid relaxation (how long it takes the fluid to return to its rest state) to the characteristic time of the flow or deformation. High Weissenberg numbers indicate dominant elastic effects, while low Weissenberg numbers indicate dominant viscous effects. The work of Min et al., explored different Weissenberg numbers at bulk Reynolds numbers. Their work observed that a sizable amount of drag reduction happens when the polymer's relaxation time is sufficient to transfer elastic energy from the near-wall region to the buffer or log layer. In contrast, when the relaxation time is insufficient for this transport, the elastic energy obtained near the wall is released there, resulting in no change in drag Min et al.. In a similar manner, the study by Li et al., investigates in depth how rheological factors relate to the observed drag reduction in turbulent channel flows. In their study, he investigated the dynamics of polymer-induced drag reduction up to the maximum drag reduction (MDR) limit using a comprehensive DNS approach. Li et al. utilized the FENE-P and Oldroyd-B, to describe the behavior of polymer chain dynamics during flow. In this study, it was remarked the need for significant polymer chain extensibility combined with high Weissenberg numbers to achieve appreciable levels of drag reduction. As it is common in computational simulations, Li et al. emphasizes the necessary computational domain lengths. He remarks that reliable results require a large computational domain length, on the order of 10^4 wall units. The main point in Li et al. study, was its focus on the correlation between the polymer body force and velocity fluctuations. The study discovered a positive correlation between

stream-wise velocity and polymer body force. This shows that the stream-wise velocity fluctuations were being increased by the viscoelastic force. The study by Li et al., sheds light on how rheological variables and polymer-induced drag reduction interact in turbulent flows. The study sheds light on the dynamics of polymer additives in turbulent channel flows and their significant impact on drag reduction through meticulous DNS simulations and in-depth statistical analysis.

Similarly, Thais et al. places a strong emphasis in understanding the impact of long polymer chains on the drag reduction in turbulent flows. Their study study offers a comprehensive analysis of the turbulent channel flow of a viscoelastic fluid. A notable discovery made in their study, was that the introduction of viscoelastic fluids resulted in an approximately 60% drag reduction across all tested Reynolds numbers when mixed with Newtonian flows. In their paper, Thais et al. discuss the effective viscosity hypothesis proposed Lumley original phenomenological description. Their study's DNS data showcase the behavior of the mean wall-normal conformation tensor component, aligning with Lumley description. Using DNS, Thais et al. studies turbulent channel flows of both Newtonian and viscoelastic fluids across an array of Reynolds numbers, spanning from $Re_\tau = 180$ to 1000. The present study uses Thais et al. DNS data as a benchmark for validating its findings.

Reynolds-Averaged Navier–Stokes (RANS)

In their study, Pinho et al. develops a RANS equation framework for modeling polymer-induced turbulent drag reduction by utilizing the FENE-P constitutive relationship to describe fluid rheology. A key aspect of their study, is the correlations between flow and polymer conformation variables, where Pinho et al. includes these turbulent correlations into a single-point k - ϵ model, which later, when compared with DNS data, reflects the efficacy of the closure approximations. Further on, Pinho et al. develops a robust framework for

turbulence closures, specifically for viscoelastic fluids conceptualized through the FENE-P rheological model.Pinho et al. highlights the deliberate inclusion of two viscoelastic terms in the transport equations of turbulent kinetic energy: the viscoelastic stress work and the viscoelastic turbulent transport term. Their work culminates in a robust k - ϵ model that is specialized for low turbulence Reynolds numbers.

Iaccarino et al. breaks ground in their research, presenting a new approach towards modeling friction drag reduction induced by polymers in turbulent wall-bounded flows. In their study, the elliptic relaxation model is adjusted to account for the new Reynolds stress equilibrium resulting from the inclusion of elastic polymer chains into the fluid dynamics. The model captures the heightened damping effect on turbulent fluctuations by altering the pressure–strain redistribution term. One of the key factors in their research is the representation of polymer solutions through the FENE-P model. Iaccarino et al. provided insight on the creation of an engineering model for predicting turbulent flows in polymer solutions. The FENE-P model is the foundation for modeling the fluid, with viscoelastic polymeric stresses integrated into the governing equations. They use the k - $\epsilon - v^2$ - f turbulence model as a framework, a four-equation eddy viscosity closure designed exclusively for Newtonian fluids. Their alteration introduces viscous damping dependent on the presence of polymers. The most important aspect of Iaccarino et al. work is the alignment of their channel flow predictions with DNS data. Their model, proves to be an indispensable asset in understanding polymer-induced drag reductions in turbulent flows. Emphasizing the model's efficiency and accuracy to replicate DNS results, Iaccarino et al. highlight its computational attractiveness when compared to the highly more expensive DNS models.

Masoudian et al. takes a similar approach to develop a a tensorially consistent near-wall four equation model to model turbulent flow of dilute polymer solutions. In their study, they develop closures in the framework of the k - $\epsilon - v^2$ - f turbulence model for the vis-

coelastic stress work, the viscoelastic destruction of the rate of dissipation, the viscoelastic turbulent viscosity, and the interactions between the fluctuating components of the conformation tensor and of the velocity gradient tensor terms. In their approach, Masoudian et al. follows the procedure proposed by Iaccarino et al. to account for the polymer shear stress term in the Reynolds averaged momentum equation, and a turbulent viscoelastic viscosity is introduced to calculate the polymer shear stress in a Boussinesq relationship, which is consistent with current DNS and independent DNS simulations. The work of Masoudian et al. is currently the most appealing option for a RANS viscoelastic drag reduction simulation, it resembles impeccably with DNS data concerning mean velocity, turbulent kinetic energy, and viscoelastic stresses across all drag reduction spectra.

The study developed by Azad et al., centers around the viscoelastic RANS turbulence model, employing the FENE-P constitutive model to characterize the polymer solution's viscoelastic properties within the k - $\epsilon - v^2$ - f framework. Azad et al. used the works of Masoudian et al. and Iaccarino et al. as a stepping stone to further research viscoelastic properties. The model was subjected to various parameters during testing, including Reynolds and Weissenberg numbers, maximum polymer extensibility, and polymer concentration. The model exhibited a robust agreement with DNS data within the range of moderate to high Reynolds numbers. In their study, Azad et al. highlight the limitations of the viscoelastic RANS turbulence model. These limitations include a decrease in accuracy when running at low Reynolds numbers when encountering low L^2 values and some challenges with accuracy at very high polymer concentrations. In conclusion, the study conducted by Azad et al., offers a thorough examination of a newly developed turbulence model, while acknowledging its limitations.

Khambhampati and Handler study adressed the instabilities in viscoelastic fluids, even at low Reynolds numbers, which can give rise to a complex phenomenon termed as elastic tur-

bulence. In their study, they investigate a particular phenomenon known as von Kármán swirling flow, utilizing the finitely extensible nonlinear Peterlin model to replicate the behavior of a sparsely distributed polymer solution. A key feaute they implemented was the employment of a log-conformation technique, a crucial component in the execution of these simulations, was essential in resolving the high Weissenberg number problem, a difficulty frequently encountered in the research of viscoelastic flows Khambhampati and Handler.

In conclusion, this literature review is centered around many studies. From looking at turbulence models and their applications in several circumstances, to experimental studies of drag reduction, to the effects of injection angles and slots, as well as the concentration of polymer solutions. Direct Numerical Simulations (DNS) and Reynolds-Averaged Navier-Stokes (RANS) models were emphasized in particular for their usefulness in predicting complex flow characteristics. Experimental research has been essential in giving empirical validation and helping to improve these models in addition to computational methods. The understanding of viscoelastic and turbulent flow dynamics has been expanded thanks to this combination of theoretical modeling, numerical simulations, and experimental trials.

1.3 Problem Statement

CFD has emerged as the principal tool in the study and analysis of fluid flows. Although the addition of polymers to turbulent flows of Newtonian fluids has been recognized to significantly reduce turbulent friction drag, the precise development of a turbulence model that characterizes viscoelastic flows has continuously been a challenge that confronts researchers around the globe. The advances in viscoelastic models, like the FENE-P model, have represented the behavior of these fluids. In spite of that, their direct numerical simulations (DNS) have proven to be computationally intensive and costly. This has driven the development of Reynolds Averaged Navier-Stokes (RANS) models, with the latest model by Masoudian et al. showing promising agreement with DNS data.

The problem that this research aims to address is the challenge surrounding the use of polymers in turbulent flows of Newtonian fluids to decrease drag. This problem is approached in three primary fronts.

1. Theoretical Fluid Dynamics Analysis: Although there is a fundamental comprehension of fluid dynamics, it is essential to conduct a theoretical analysis that is customized to the specific conditions and limitations of the hydrodynamics laboratory. The understanding of theoretical predictions of flow rate is needed. This results in a need for a model capable of forecasting the dynamics of the fluid flow within this particular setting.

2. Experimental Fluid Dynamics Analysis: The practical investigation of the lab's channel flow system becomes crucial once theoretical expectations are established. In order to compare these results with theoretical predictions, an experimental analysis must be conducted in order to capture the real world behaviors of the flow rate in the hydrodynamics lab. To achieve accuracy and repeatability, careful experiment design and execution are required.

3. Evaluation of the Viscoelastic RANS Turbulence Model: The model proposed by Masoudian et al. constitutes an important step forward in our computational understanding of the phenomenon. Nevertheless, a thorough evaluation is necessary to determine the actual reliability of this viscoelastic RANS turbulence model, particularly when it comes to accurately predicting values related to Drag Reduction (DR). It is crucial to determine the accuracy, relevance, and limitations of this model when employed under diverse circumstances. In order to evaluate the viscoelastic RANS turbulence model, the CFD software Open Source Field Operation and Manipulation (OpenFOAM) was used.

In conclusion, the challenges outlined above highlight the importance and complexity of our investigation. Analysing the results from theoretical predictions and empirical observations will enhance our understanding of fluid dynamics in a controlled environment. Furthermore, the evaluation of the viscoelastic RANS turbulence model developed by Masoudian et al. represents an insight on the behaviour that polymer has on Newtonian fluids. This evaluation will establish the model's accuracy, applicability, and potential to be a reliable tool for comprehending viscoelastic turbulent flows.

1.4 Research Objectives

The goal of this study is to deeply understand the fundamental principles of fluid dynamics, perform both theoretical and experimental analyses of the hydrodynamic laboratory in Virginia Tech, and to evaluate the viscoelastic RANS turbulence model developed by Masoudian et al. in predicting drag reduction values. The research is driven by a combination of theoretical knowledge and practical implementation, with the objective of developing a model that can be applied in real-world scenarios. The goal is supported by specific objectives, which are:

- Understanding Fundamental Principles of Fluid Dynamics
- Development of Theoretical Model & Analysis of Hydrodynamic Laboratory
- Experimental Analysis of Hydrodynamic Laboratory
- Implementation of Viscoelastic RANS Turbulence Model in OpenFOAM
- Evaluation of Viscoelastic RANS Turbulence Model
- Simulation and Analysis of the Implemented Model
- Validation of the Viscoelastic RANS Turbulence Model

The objectives presented in this statement delineate the taken research path, which requires a comprehensive understanding of both theoretical and experimental components. The success of the research heavily relies on each step, as they are all crucial in paving the way for significant contributions to the fields of fluid dynamics, computational modeling, and the understanding of polymeric solutions. In order to achieve these objectives, a broad approach is necessary. This approach involves combining profound theoretical knowledge, thorough experimental investigations, and advanced computational fluid dynamic techniques.

1.5 Thesis Outline

The thesis is organized as follows: it initiates with the Methodology Chapter (2). This chapter contains the Experimental Setup and Procedure section (2.1), which delineates setup in the hydrodynamics laboratory and the procedure to operate it. The Theoretical Model Development section (2.2) follows, explaining the specific Assumptions concerning the underlying physics, and the Theoretical Model Numerical Analysis (2.3), outlines the comprehensive process to determine flow rate.

Within the Methodology Chapter, the Experimental Model Methodology section (2.4) expands on the procedure employed for gathering experimental data. A significant portion of the chapter is devoted to the CFD Analysis using OpenFOAM (2.5). This includes OpenFOAM and the C++ Language (2.5.1), outlining the foundational software; The Structure of an OpenFOAM Case (2.5.2), describing the typical folders included in an OpenFOAM case; and the Implementation of RANS Viscoelastic Turbulence Model (2.5.3). This subsection carefully details the formulation of the Reynolds-Averaged Navier-Stokes (RANS) turbulence model for viscoelastic fluids and its meticulous adaptation within the OpenFOAM environment, along with an exploration of Governing Equations (2.5.4), Grid Study and Boundary Conditions (2.5.5), and Solver Selection and Numerical Schemes (2.5.6).

The next chapter, Theoretical Model Results and Analysis (3), focuses on the outcomes and interpretation of the theoretical model results, followed by the Experimental Results and Analysis (4), which provides an exposition of experimental model findings. Section (5) presents a detailed examination of the Viscoelastic Turbulence Model Results, which includes a thorough Model Validation (5.1) segment.

The concluding chapter, Conclusion and Future Work (6), encloses the research with a Summary of Findings, and Recommendations for Future Work.

Chapter 2

Methodology

2.1 Experimental Setup and Procedure

The utilized facility in this dissertation refers to the Hydrodynamics Laboratory located in the basement of Randolph Hall at Virginia Tech. The hydrodynamics laboratory houses a creative, gravity powered water channel system known as the Hydrodynamics Water Channel. The system is a combination of multiple components including three interconnected water tanks, a main water tank container, connecting PVC pipes carefully designed to work solely with gravity, a water channel and a discharge bin that is equipped with a scale for data collection.

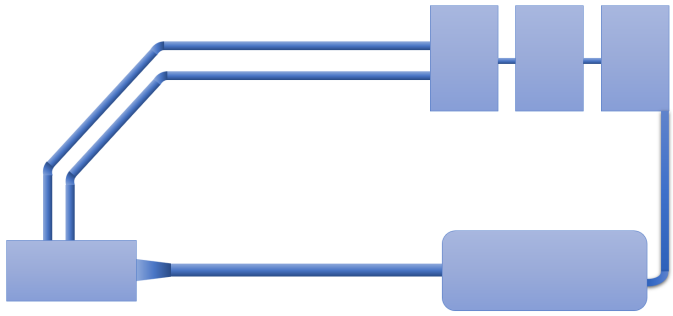

Figure 2.1: Hydrodynamics Laboratory Top View

Figure 2.1 depicts visually the top view of the Hydrodynamics Laboratory at Virginia Tech.

Figure 2.2: Hydrodynamics Laboratory Front View

Figure 2.2 depicts visually the front view of the Hydrodynamics Laboratory at Virginia Tech.

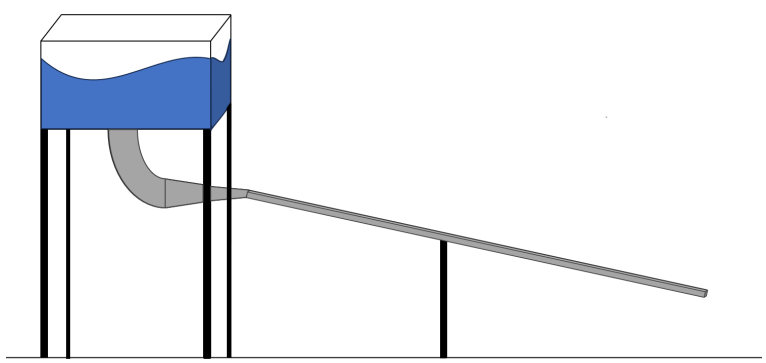

Figure 2.3: Hydrodynamics Laboratory Side View

Figure 2.3 depicts visually the side view of the Hydrodynamics Laboratory at Virginia Tech.

In accordance with the system's flow, the water tanks are placed as the initial component. Each tank is set at a height of 5 meters, and the tanks are linked together to create a cascade effect. Water overflows into the second tank after flowing into the first tank and filling it halfway. When the second tank reaches halfway capacity, it begins to overflow into the third. This arrangement ensures a consistent and uninterrupted flow of water, which is crucial for many of our experiments that require a steady state to produce accurate results. When the third tank is halfway full, the water is then transferred through PVC circular pipes to a main water tank that's slight lower at 3.5 meters. The height difference its crucial for the water to flow naturally from the thanks to the main reservoir without the use of any mechanical device.

The main water container is connected to the water channel via a ball valve which allows the flow to be controlled. The opening and closing of this device we can regulate the water flow. Once the ball valve is open, the water travels through an elbow and a ball socket joint before entering the water channel. The water channel, the main component in our research's setup, has an extended rectangular shape with measurements of 4 inches in width, 0.4 inches in height, and 159 inches in length. These proportions have a particular 10:1 aspect ratio of width to height, which has a substantial impact on the resulting flow dynamics. Furthermore, the channel has two strategically placed slots at the bottom. These slots allow for the introduction of a solution into the existing flow, simplifying investigations that require the addition of a secondary fluid or a tracer. A transparent test portion at the channel's terminal segment provides a clear view of the flow dynamics within the channel. This clear section facilitates direct visual observations. Its long size allows us to observe and study the water's flow patterns over an extended distance. We also have the ability to adjust the channel's inclination using a hydraulic bottle jack, enabling us to create a wide range of flow scenarios.

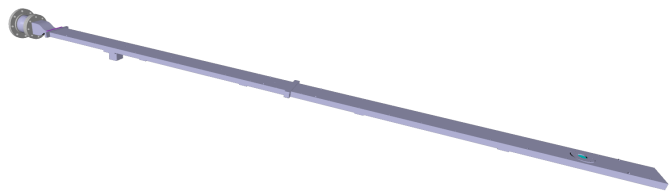

Figure 2.4: Hydrodynamics Laboratory Water Channel

Figure 2.5: Water Channel Y+

Figure 2.6: Water Channel Y-

Figure 2.7: Cross Section X+

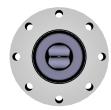

Figure 2.8: Cross Section X-

Figure 2.4 showcase an overall view of the water channel. This view offers a entire overview of the setup which includes the ball socket joint entrance and the test section at the end of the channel. Figures 2.5 and 2.6 display the Y+ and Y- views of the channel. These perspectives are significant to observe the length of the channel. Finally, figures 2.7 and 2.8 display the cross sectional areas (X+ and X-) of both the entrance and exit of the channel. In figure 2.7 the vast majority of the geometry can be appreciated. The hydrodynamic system incorporates a channel exhibiting an aspect ratio of 10:1, denoting the width to height.

Ultimately, to maintain coherence with the system's flow, the water end in a discharge bin with the possibility of being pumped back up to the water tank. The discharge bin is placed on top of a scale to measure the weight of the discharged water with the purpose of computing the water channel flow rate.

In terms of procedure, in order to operate the water channel, these are the following steps that need to be followed:

The initial step in our experimental procedure requires the preparation of our data recording system. This requires connecting the weight scales to the power supply and calibrating it, ensuring that the display indicates zero. Following this step, it is essential to make sure that the ball valve connecting the water supply and the connecting tanks, is in a closed position. Simultaneously, one must verify that the ball valve linking the main container and the water channel is also securely closed. These preemptive measures help control the water flow during the initial setup phase and prevent premature water discharge. Once the initial precautions are taken, the following step is to ascend the ladder to access the primary water supply. Here is where to initiate the water flow into the system by opening the water supply. With the water supply valve open, the water will begin its downward descent, filling the tanks progressively due to gravitational pull. To avoid overfilling the tanks, this operation must be continuously monitored. As a result, the water supply must be manually cut off before the tanks reach their volumetric limit. As the filling procedure is completed, the water will eventually fill the main tank, indicating that the water channel is ready for use. At this point, the hydraulic bottle jack can be used to modify the channel angle of inclination to the required level. This modification allows us to modify the gradient of the water flow, resulting in a controlled variation in the flow dynamics. The next step involves opening the ball valve that regulates the flow of water from the main tank to the channel. When you are certain that the system is ready for data collecting, open this ball valve. As a result, the water will begin to flow through the channel and eventually end up in the discharge bin. As an optional final step. If the channel is operated with solely water, the water in the discharge bin can be pumped back up to the water tanks by the use of a small pump.

Finally, our Hydrodynamics Laboratory's gravity-operated water channel system is the result

of a combination of precision engineering and fluid dynamics, and it is designed to provide a wide range of flow scenarios required for high-impact hydrodynamic experiments. The one-of-a-kind design incorporates a cascade tank system, a regulated flow mechanism, a flexible channel with a characteristic 10:1 aspect ratio, and a data collecting system to allow for a thorough and in-depth examination of fluid dynamics concepts. When the extensive setup procedures and methodology are followed precisely, the findings are robust, dependable, and replicable.

2.2 Theoretical Model Development

Considering the complexity of the system under investigation, the development of a diligent theoretical model to predict fluid dynamics within the hydrodynamic system is necessary. This model, which is based on verified hydrodynamic principles and empirically developed equations, will allow the flow rate inside the water channel system to be predicted. The model takes into account the complete flow process, from the raised tanks to the pipes and elbows, the ball and socket joint, and the water channel. We build our model on a set of rational assumptions and well defined system parameters to assure the accuracy of our theoretical predictions.

2.2.1 Assumptions

Several reasonable assumptions have been made in order to develop a theoretical model for the current fluid dynamics investigation. These assumptions, which have their basis in traditional hydrodynamics theory, allow for analytic modeling of the system as well as precise prediction.

Steady, Incompressible, and Fully Developed Flow

The flow of water within the system is assumed to be constant, signifying that flow properties at any given point within the system do not alter over time. In addition, water is considered incompressible due to the low velocities and high pressures associated with our laboratory's parameters.Finally, it is assumed to be a fully developed flow, that is, a flow in which physical properties change only in the direction of the flow and not across the cross-section. According to Batchelor, a fully developed flow is a standard approach for the accuracy of

flow in long pipelines and channels.

Assuming Turbulent Flow

According to Pope, turbulent flows are characterized by chaotic, three-dimensional vortical motion, which increases momentum, heat, and mass transport. Due to the randomness inherent to turbulence, it is difficult to model accurately. However, its substantial impact on fluid flow behavior, particularly in terms of energy losses and pressure decreases, cannot be disregarded.

The assumption of turbulent flow in our model is supported by the calculated Reynolds number, and is based on the characteristic nature of the fluid flow in our experimental setup. Reynolds number (Re) is widely used in fluid dynamics to predict the beginning of turbulence. It is calculated using the formula

$$R_e = \rho V D / \mu \tag{2.1}$$

where ρ represents the fluid density, V represents the fluid velocity, D represents the hydraulic diameter of the conduit, and represents the fluid viscosity Fox et al.

Following the successful calculation of the Reynolds Number flowing in the pipes, we find that the high velocities coupled with the diameters of the pipes result in a turbulent flow. The corresponding Reynolds number for our system is significantly greater than 4000, the typical threshold for turbulent flow White and Majdalani. Therefore, the assumption of turbulent flow is not only justifiable but also essential for accurately modeling the fluid dynamics of our system. The assumption of a turbulent flow, allows the utilization of a Moody Chart first proposed by Moody shown in figure 2.9, to incorporate the effects of pipe roughness and flow turbulence on pressure loss

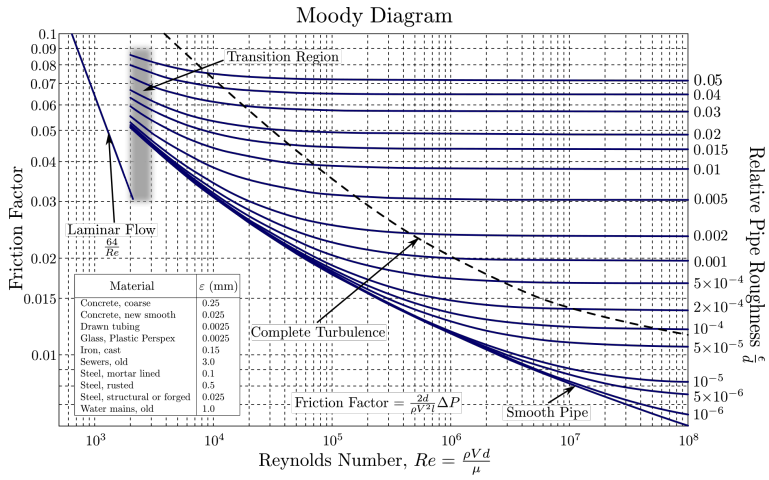

Figure 2.9: Moody Diagram

Accounting for Minor Losses

In the analysis of the flow,the minor losses refer to pressure or head losses caused by fluid whcih encounters couplings, bends, valves, contractions, expansions, and other localized disturbances within a piping system. These components can disrupt the fluid's consistent and streamlined flow, leading to additional energy losses. We include in our model the impact of minor losses, such as those at the entrance and exit of the pipelines and those resulting from sudden expansions or contractions. According to Munson et al., these losses have a significant impact on flow characteristics and system performance, particularly in systems with multiple connectors and varying cross-sectional areas.

Account for Hydrostatic Pressure and Gravitational Effects

Hydrostatic pressure is an essential concept in fluid dynamics, particularly for gravity-driven flows. It is the fluid pressure exerted at equilibrium by the force of gravity.

Due to the varied height differences within the system, gravity's effects are taken into ac-

count, and the fluid pressure is considered hydrostatic. This is a common method for handling flows with substantial elevation variations according to White and Majdalani.

Constant Fluid Properties

According to White and Majdalani, fluid properties like density and viscosity are frequently affected by variables like temperature and pressure. However, for many engineering applications that involve water under ambient conditions, these properties can be treated as constants. For the purpose of this model, we assume that the fluid properties remain constant. For water at a temperature of 20°C, the density ρ is considered to be 998.2 kg/m^3 and the dynamic viscosity μ is considered to be 0.001002 $Pa.s$

2.3 Theoretical Model Numerical Analysis

Understanding the fundamentals of fluid dynamics, particularly the behavior of water under the influence of gravity and friction, is essential for countless civil and environmental engineering applications. For this part of our research, we studied and developed a theoretical model that predicted the flow rate of the water channel. The purpose of this part of the study is to analyze a specific the system consisting of a gravity-fed water flow from a container through a series of components. As mentioned above, when the water reach the main water tank it remains at rest, this is where the theoretical numerical analysis will begin. Our methodology for this analysis incorporates several fundamental fluid mechanics principles. These include Torricelli's Law for calculating the initial velocity of the water as it exits the container, the Darcy-Weisbach equation for calculating frictional losses in the pipe, and Bernoulli's equation for accounting for changes in velocity and pressure as the water flows through the channel. In addition, minimal losses are accounted for due to the presence of the valve, elbow, and ball-and-socket joint.

2.3.1 Comprehensive Process to Determine Flow Rate

To begin at the point of origin of the liquid, we will begin with the discharge that comes from the container.The first fluid mechanics principle considered is Torricelli's Law. Torricelli's Law defines the rate at which an incompressible, non-viscous fluid exits a container through a hole with a sharp edge under the influence of gravity. It states that the velocity of fluid exiting the cavity under the force of gravity is proportional to the square root of the fluid's height above the center of the hole D'Alessio.

Torricelli's Law is represented mathematically in equation 2.2

$$V = \sqrt{2gh} \tag{2.2}$$

where V is the outflow velocity, g is the gravitational acceleration and h is the fluid column height above the opening in meters. In our setup, h was measured as the vertical distance between the floor of the tank and the top of the water column, which was 3.5 meters. We calculated the initial velocity of water as it begins to flow out of the container by substituting these values into the equation.This velocity was then used as the starting point for subsequent fluid flow calculations through the pipe, elbow, ball-and-socket joint, and inclined channel.

In our system, the ball valve is the first component water encounters as it leaves the container. The function of a valve is to control the flow rate, and in doing so, it causes energy loss due to abrupt variations in flow direction and velocity Munson et al.. These losses are referred to as minor losses, in spite of the fact that they can become significant in large systems with numerous components.

To calculate the loss caused by the ball valve, loss coefficients were utilized. A component's loss coefficient (K) is a dimensionless number that describes the energy loss associated with

that component. Typically, this coefficient for a completely open ball valve is around 0.05 Idelchik.The head loss due to the ball valve is mathematically represented in equation

$$h_{valve} = K_{valve}\frac{V^2}{2g} \tag{2.3}$$

where h_{valve} is the head loss due to the valve, K_{valve} is the loss coefficient for the ball valve, V is the velocity of water and g is the acceleration due to gravity.

As water passes the ball valve, it enters a pipe that leads to the elbow. Even though the conduit is straight, frictional losses occur due to the roughness of its internal surface. These are considered minor losses, but in lengthy pipelines, they can have a substantial impact on the total energy Idelchik. The Darcy-Weisbach equation can be used to calculate frictional losses for a given pipe's length and a known fluid velocity and is mathematically represented in equation 2.4

$$h_{pipe} = f * \frac{L}{D}\frac{V^2}{2g} \tag{2.4}$$

where h_{pipe} is the head loss due to the pipe, f is the Darcy friction factor, L is the length of the pipe and D is the diameter of the pipe.

The friction factor, is a vital parameter in fluid dynamics because it quantifies the effect of frictional resistance on fluid flow. It is dimensionless and is dependent on both the characteristic of the fluid, and the fluid conduit (such as the pipe's diameter and surface) White and Majdalani. The Darcy friction factor (f) is determined by the Reynolds number of the flow and the relative pipe roughness. It can be approximated using the Moody Diagram showed in figure 2.9. Using the known parameters, including the pipe's length and diameter, and the calculated velocity, we were able to estimate the frictional losses in our system caused by the pipe.

After passing through the straight pipe, the fluid flow is redirected by an elbow at a 90-

degree angle. This abrupt change in direction significantly disrupts the flow, resulting in a significant increase in energy loss, also known as minor losses. The head loss through an elbow can be estimated with an expression similar to that used for the ball valve and is mathematically represented in equation 2.5.

$$h_{elbow} = K_{elbow}\frac{V^2}{2g} \tag{2.5}$$

The elbow loss coefficient K_{elbow} can vary significantly dependent on the elbow's precise geometry and flow rate. For a our 90-degree elbow in entirely turbulent flow, $K_{elbow} = 0.45$ is a reasonable estimate according to Idelchik.

After the elbow, the water flow encounters a ball-and-socket joint. Due to the complex geometry and potential for turbulent flow conditions within the joint, it introduces additional minor losses to the system. This rotational alignment disrupts the fluid's flow path and generates local turbulence, which increases head loss White.The head loss through the ball socket joint can be estimated with an expression similar to that used for the elbow and is mathematically represented in equation 2.6.

$$h_{joint} = K_{joint}\frac{V^2}{2g} \tag{2.6}$$

The loss coefficient for the joint K_{joint} is estimated based on similar fitting types. For this study, we assumed $K_{joint} = 0.9$, a typical value for complex fittings under turbulent flow conditions Idelchik.

The water flow eventually enters the incline rectangular channel after overcoming the losses caused by the valve, pipe, elbow, and joint. The water channel was inclined in a range of 10 - 15 degrees to the horizontal during this experiment. Given that our flow is gravitationally downward, it makes sense to anticipate that the velocity will rise relative to the entrance

velocity. This was calculated using the energy equation in its general form, 2.8 and taking the channel inclination into account. To complete the theoretical head losses, the head loss due to the channel was computed using equation 2.7.

$$h_{channel} = f * \frac{L}{D}\frac{V^2}{2g} \tag{2.7}$$

After assumptions, rearrangement and substitution, equation 2.8 becomes equation 2.9.

$$\frac{P_1}{\rho g} + \frac{V_1^2}{2g} + z_1 + h_pump = \frac{P_2}{\rho g} + \frac{V_2^2}{2g} + z_2 + h_{losses} \tag{2.8}$$

$$V_2 = \sqrt{V_1^2 + 2g(h_1 - h_2 - h_{valve} - h_{pipe} - h_{elbow} - h_{joint} + h_{channel})} \tag{2.9}$$

Following the computation of the exit velocity V_2, the cross-sectional area A_2 of the channel and the exit velocity were used to calculate the flow rate Q_2 depicted in equation 2.10.

$$Q_2 = A_2 V_2 \tag{2.10}$$

We have thoroughly covered the step-by-step process used to calculate the flow rate of water leaving an elevated container, passing through a valve, pipe, elbow, and ball and socket joint, and then flowing along an inclined channel in this theoretical model numerical analysis. In order to account for various energy losses and the effect of the channel's inclination on the fluid's velocity, this elaborate process required a thorough understanding of and application of fluid dynamics principles, particularly the energy equation. The Theoretical Model Results and Analysis section (3), presents and discusses the findings of these theoretical calculations. The correctness of our model will be evaluated here, as well as any potential gaps in our

theoretical knowledge or the design of our experiments, through comparison of these values with experimental data.

2.4 Experimental Model Methodology

2.4.1 Procedure

To maintain uniformity and guarantee accurate results, the experimental procedure was carefully developed and meticulously carried out. We broke down the procedure into a number of smaller steps, each of which is necessary to getting a precise flow rate measurement.

First, the ball valve was fully opened to allow water to start flowing through the system after establishing the beginning conditions. The start of each experimental run was signaled by the appearance of this flow. The valve was opened and a timer started at the same time. Since each run in these tests had a set duration to ensure consistency across all trials, the timing component was crucial. Weight Scales A and B were set to zero before the 10 trial procedure began. At the beginning and end of each 30 second interval, the weights were measured. This 30 second time limit was chosen to enable several readings throughout each trial as well as sufficient water volume collection for measurements. The beginning and final weights were provided by the scales, and they were carefully recorded. Then, for each scale, we determined the difference between the final and initial weights. This effectively gave us the volume of water that was discharged from the channel in the allotted 30 seconds. We summed the weight discrepancies from the two scales to determine the total weight of the water discharged. For each set of conditions, the method was carried out ten times. In order to reduce the impact of any irregularities or outliers that may have occurred during individual trials.

Once the 10 trial procedure was completed, each trial had an average change in mass ($\Delta m_{trialnumber}$). Utilizing that individual change in mass, equation 2.11 was used to compute the flow rate.

$$Q_{trialnumber} = \frac{\Delta m_{trialnumber}}{\Delta t} \tag{2.11}$$

where (Δt) is the time interval (30 seconds in our experiment), and (Δm) is the change in mass (for our purposes, equivalent to the change in weight given constant gravity).

Each trial resulted in a flow rate out of the channel. These results were then averaged to yield a final experimental flow rate for the given conditions. The experimental flow rate and the channel's cross-sectional area were then used in equation 2.10 to calculate the water's ultimate experimental exit velocity.

In conclusion, the methodology presented in this section offered a methodical, reliable, and repeatable procedure for determining the water flow rate through the inclined channel system. The reliability and validity of our findings were further improved by using averaged data from several experiments. Section 4 will present these experimental findings and contrast them with our theoretical results.

2.5 CFD Analysis using OpenFOAM

The computational portion of this research makes use of OpenFOAM software, a vigorous open-source tool used for computational fluid dynamics. OpenFOAM is grounded and based on C++ as its programming language.

2.5.1 OpenFOAM and The C++ Language

Together, they provide an alternative to theoretical and experimental approaches when dealing with fluid flow analysis. Being an open source software, OpenFOAM, offers a wide variety of different cases and settings making it the ideal candidate for this research purposes. One of the many advantages of using OpenFOAM for this dissertation, as opposed to other commercial software, lies in its versatility when it comes to extending, adapting and/or customizing turbulence models. OpenFOAM allows users to access and modify the source code of these models. This feature is instrumental in research where standard turbulence models might not fully capture the physics of the problem at hand, such as the complex interactions between turbulent flow and polymeric additives in our study.

In this study, we leverage this powerful feature of OpenFOAM to develop a custom turbulence model that accurately captures the impact of various polymeric solutions on drag reduction. The custom model is implemented as a C++ class, extending one of the standard turbulence models in OpenFOAM, with modifications to account for the effects of the polymeric additives. This approach provides us with a powerful, flexible tool to explore and simulate the complex phenomenon of drag reduction by polymeric additives.

Understanding the OpenFOAM case's structural organization is crucial for effective implementation and problem solving. A problem can be solved using the information and

instructions found in an OpenFOAM case.

2.5.2 The Structure of an OpenFOAM case

The standard OpenFOAM case, consists of three main directories. The constant, system and 0.orig folders.

Constant: Acording to Jasak, All of the constant characteristics needed by the case are contained in this directory. The files ”transportProperties,” ”turbulenceProperties,” ”g” (for gravity), and ”polyMesh,” which gives details about the mesh, are often included.

System: The control files that specify how the case will be run are located in this directory. The ’controlDict’ (which regulates how the case is executed), ’fvSchemes’ (which describes the discretization schemes), and ’fvSolution’ (which establishes the solver parameters) are usually the key files located here Jasak.

0.orig: All of the variables that need to be solved have their initial conditions stored in this location. It specifies the field values at the start of the simulation for time-dependent situations Jasak

2.5.3 Implementation of RANS Viscoelastic Turbulence Model

As stated in section 1.2 of this research, numerical simulation of dilute polymer solutions has been a great field of study for many researchers. The viscoelastic model FENE-P (Finitely Extensible Nonlinear Elastic-Peterlin) is frequently used to explore these fluids because it takes the effect of chain extensibility into account. As seen in 1.2, authors like Ptasinski et al., Min et al., Thais et al. amongst others, identified the intricate process of turbulent drag reduction in polymer solutions using direct numerical simulation (DNS). Due to the

high costs and impracticality that comes with DNS, Iaccarino et al. and Pinho developed Reynolds Averaged Navier Stokes (RANS) models. Based on the $k - \epsilon - \overline{v^2} - f$ turbulence model with new closures, Masoudian et al., offered a model that is comparable to the one Iaccarino et al. presented. The results of this model, as opposed to the ones of IIaccarino et al., were in greater agreement with DNS data due to the application of several precise closures for the nonlinear turbulence terms.

In conclusion, a wide variety of models, ranging from the frequently used FENE-P method to the sophisticated analyses offered by DNS, have been used to examine diluted polymer solutions. Although the latter provided more in-depth understanding of turbulent drag reduction, its expensive costs prompted the creation of more useful RANS models. Masoudian et al.'s ground-breaking study, which uses the $k - \epsilon - \overline{v^2} - f$ turbulence model with new closures, represents a substantial advancement by producing results that are more in line with DNS data.

2.5.4 Governing Equations

RANS Viscoelastic Turbulence Model

As mentioned above, the viscoelastic turbulence model utilized in this research was developed by Masoudian et al.. In which the description of dilute polymer solutions is based on the Finitely Extensible Nonlinear Elastic-Peterlin (FENE-P) constitutive equation. The momentum equation for an incompressible viscoelastic flow is denoted in equation 2.12.

$$\rho\frac{\partial u_i}{\partial t} + \rho u_j\frac{\partial u_i}{\partial x_j} = -\frac{\partial p}{\partial x_i} + \rho\frac{\partial}{\partial x_j}\left[\nu_s\frac{\partial u_i}{\partial x_j}\right] + \frac{\partial \tau_{ij}^p}{\partial x_j} \tag{2.12}$$

The solvent's density and viscosity are represented by ρ and ν_s in equation 2.12.Viscous and polymer stresses are the second and third terms on the right side of 2.12. The last term in equation 2.12 is the FENE-P model-based definition of polymer stress which its characterized in equation 2.13

$$\tau_{ij}^p = \frac{\eta_p}{\lambda}(C_{ij}f(C_{kk}) - \delta_{ij}) \tag{2.13}$$

Where η_p and λ represent the polymer intrinsic viscosity and relaxation time and C_{ij} represent the conformation tensor. The term $f(C_{kk})$ is the Peterlin function defined as:

$$f(C_{kk}) = \frac{L^2 - 3}{L^2 - C_{kk}} \tag{2.14}$$

In equation 2.13, L^2 represents the maximum extension of the polymer chains and C_{kk} represents the normalized elongation of polymer chains with respect to the characteristic polymer length in the equilibrium no flow state.

The conformation tensor obeys a hyperbolic differential equation of the form:

$$\frac{\partial c_{ij}}{\partial t} + u_k \frac{\partial c_{ij}}{\partial x_k} - c_{ik}\frac{\partial u_i}{\partial x_k} - c_{ik}\frac{\partial u_j}{\partial x_k} = \frac{1}{\lambda}(\delta_{ij} - f(C_{kk})C_{ij}) \tag{2.15}$$

After Reynolds averaging the instantaneous equations, the momentum equation becomes

$$\rho\frac{\partial U_i}{\partial t} + \rho U_j \frac{\partial U_i}{\partial x_j} = -\frac{\partial P}{\partial x_i} + \rho\frac{\partial}{\partial x_j}\left[(\nu_s + \nu_t)\frac{\partial U_i}{\partial x_j}\right] + \frac{\overline{\partial \tau_{ij}^p}}{\partial x_j} \tag{2.16}$$

Where U_i stands for the components of mean velocity and ν_t for turbulent viscosity. The Mean Polymer Stress is defined as:

$$\overline{\tau_{ij}^p} = \nu_{t,p}\frac{\partial U_i}{\partial x_j} \tag{2.17}$$

Where $\nu_{t,p}$ is the turbulent polymer viscosity.The governing and model equations developed by Masoudian et al. are given below:

$$\frac{\partial U_i}{\partial x_i} = 0 \tag{2.18}$$

$$\rho\frac{\partial U_i}{\partial t} + \rho U_j \frac{\partial U_i}{\partial x_j} = -\frac{\partial P}{\partial x_i} + \rho\frac{\partial}{\partial x_j}\left[(\nu_s + \nu_t + \nu_{t,p})\frac{\partial U_i}{\partial x_j}\right] \tag{2.19}$$

$$U_j\frac{\partial k}{\partial x_j} = P_k - \epsilon + \frac{\partial}{\partial x_j}((\nu_s + \frac{\nu_t}{\sigma_k})\frac{\partial k}{\partial x_j}) - \epsilon_p \tag{2.20}$$

$$U_j\frac{\partial \epsilon}{\partial x_j} = \frac{C_{\epsilon 1}P_k - C_{\epsilon 2}\varepsilon}{T_t} + \frac{\partial}{\partial x_j}((\nu_s + \frac{\nu_t}{\sigma_\epsilon})\frac{\partial \epsilon}{\partial x_j}) - E_p \tag{2.21}$$

$$U_j\frac{\partial \overline{v^2}}{\partial x_j} = kf + \frac{\partial}{\partial x_j}((\nu_s + \frac{\nu_t}{\sigma_k})\frac{\partial \overline{v^2}}{\partial x_j}) - \frac{6\epsilon}{k}\overline{v^2} - \epsilon_{p,yy} \tag{2.22}$$

$$f - L_t^2 \frac{\partial^2 f}{\partial x_j \partial x_j} = (C_1 - 1)\frac{(\frac{2}{3} - \frac{\overline{v_2}}{k})}{T_t} + C_2 \frac{P_k}{k} + 5\epsilon \frac{\overline{v^2}}{k^2} \tag{2.23}$$

$$M_{kk} + NLT_{kk} + \frac{1}{\lambda}(3 - f(C_{kk})C_{kk}) + k\frac{\partial}{\partial x_j}(\frac{\partial C_{kk}}{\partial x_j}) = 0 \tag{2.24}$$

In the equations that have been presented thus far, k and v^2 stand for turbulent kinetic energy and its wall normal component, respectively. ϵ denotes the dissipation rate, and f refers to the energy redistribution process that is an essential part of the generation of v^2. The turbulent viscosity and the new turbulent polymer viscosity in equation 2.19 are defined as:

$$\nu_t = C_\mu \overline{\nu^2} T_t \tag{2.25}$$

$$T_t = \max\left(\frac{k}{\epsilon}, 6\sqrt{\frac{\nu_s}{\epsilon}}\right) \tag{2.26}$$

$$\nu_{t,p} = \frac{\nu_p}{f(C_{kk)}} + a_1 \sqrt{\frac{L^2}{Wi_{\tau o}}} f(C_{kk})\nu_t \tag{2.27}$$

$$Wi_{\tau o} = \frac{\lambda U_\tau^2}{\nu_o}, \nu_o = \nu_p + \nu_s \tag{2.28}$$

The new source terms for FENE-P fluids in equations 2.20 - 2.28 are defined as:

$$\epsilon_p = \frac{\mu_p}{2\rho\lambda} f(C_{kk}) NLT_{kk} \tag{2.29}$$

$$\epsilon_{p,yy} = a_1 a_3 L f(C_{kk}) k f \tag{2.30}$$

$$E_p = \frac{C_{\epsilon 1}\epsilon_p}{T_t} \tag{2.31}$$

$$M_{kk} = 2\left[\frac{\lambda}{f(C_{kk}} \frac{\nu_{t,p}}{\nu_p}\left(\frac{dU}{dy}\right)^2\right] \tag{2.32}$$

$$NLT_{kk} = a_2 M_{kk} \frac{\nu_t}{\nu_o} \tag{2.33}$$

The length scale appearing in equation 2.23 is defined as:

$$L_t^2 = C_l^2 \max\left(\frac{k^3}{\epsilon^2}, C_\eta^2 \sqrt{\frac{\nu^3}{\epsilon}}\right) \tag{2.34}$$

Where the denoted terms $C_l, C_\eta, a_1, a_2, a_3$ are model constants given by Masoudian et al., and can be found listed in table 2.1.

Constant	C_μ	σ_k	σ_ϵ	$C_{\epsilon 1}$	$C_{\epsilon 2}$	C_1	C_2	C_l	C_η	a_1	a_2	a_3
Value	0.22	1	1.3	$1.4(1+0.5)\sqrt{\frac{k}{v^2}}$	1.9	1.4	0.3	0.23	70	0.02	0.16	0.15

Table 2.1: Model Constants

Flow Characteristics

In the case of fully turbulent channel flow of FENE-P fluids, the flow and rheological properties can be fully described using four dimensionless parameters. These parameters include the friction Reynolds number (Re_τ), the friction Weissenberg number ($We_{\tau 0}$), the ratio of solvent viscosity to total viscosity (β), and the maximum extension of the polymer chains (L^2). The initial three numbers are established by Masoudian et al. as:

$$Re_\tau = \frac{\rho u_\tau h}{\mu_0} \tag{2.35}$$

$$We_{\tau 0} = \frac{\rho \lambda u_\tau^2}{\mu_0} \tag{2.36}$$

$$\beta = \frac{\mu_s}{\mu_0} = \frac{\mu_s}{\mu_s + \mu_p} \tag{2.37}$$

Where λ is the relaxation time for viscoelastic solvent, h is the channel half height μ_τ is the wall shear stress velocity defined in equation 2.38 and μ_0 is the polymeric solution's total viscosity at zero shear rate.

$$u_\tau = \sqrt{\frac{\tau_w}{\rho}} \tag{2.38}$$

In order to compute the percent of drag reduced, Ptasinski et al. suggests the use of equation 2.39.

$$DR\% = \left(1 - \frac{C_{f,visc}}{C_{f,new}}\right) * 100 \tag{2.39}$$

Where $C_{f,visc}$ and $C_{f,new}$ represent the friction coefficient of the viscoelastic and Newtonian fluids, respectively, and can be computed using equation 2.40.

$$C_f = \frac{\tau_w}{\frac{1}{2}\rho U_b^2} \tag{2.40}$$

Where U_b is the bulk velocity in the channel and τ_w is the wall shear stress.

2.5.5 Grid Study and Boundary Conditions

In order to accurately describe a flow in a domain, rigorous mesh construction and the application of suitable boundary conditions are required. The following part of this research explains the exact boundary conditions used and the rigorous mesh generation process used to precisely model the flow.

Grid Study

The grid study represents an integral component of the research, which centers on the examination of a two-dimensional channel characterized by a vertical dimension of 2h and a horizontal dimension of 10h. A non uniform collocated mesh was generated employing the Finite Volume Method. A thorough grid convergence investigation was conducted with three grids with various sizes. The objective of this thorough analysis was to determine how sensitive the solution was to the mesh size. In order to assure a correct characterization of the flow, special attention was employed in the size of the cells near the walls. This is an area of often challenge due to the interaction between the fluid and solid boundaries. In order to accurately capture the near-wall turbulence effects, the height of the first mesh cell was carefully adjusted to achieve a dimensionless wall distance of y+ 1. This was obtained with OpenFOAM's Simple-grading capability which allows the geometry to be fine in crucial areas and coarser in non crucial areas. Figure 2.10 presents the the visual representation of the simple grading near the walls, illustrating how the geometry is fine-tuned in crucial areas and made coarser in non-crucial areas, using OpenFOAM's Simple-grading capability.

The grid convergence analysis was conducted by generating three distinct grids, where N_x represent the number of cells in the stream wise direction and N_y represents the number of cells in the wall normal direction. In order to simulate a 2D flow, the number of cells in the span wise direction N_z was intentionally set to one.The implementation of this constraint guarantees that the flow is accurately represented as a two-dimensional model.

Grid	$N_x * N_y * N_z$	Channel Length (L)	Channel Height (2h)
Grid 1	65 x 65 x 1	10	1
Grid 2	111 x 111 x 1	10	1
Grid 3	199 x 199 x 1	10	1

Table 2.2: Mesh Analysis

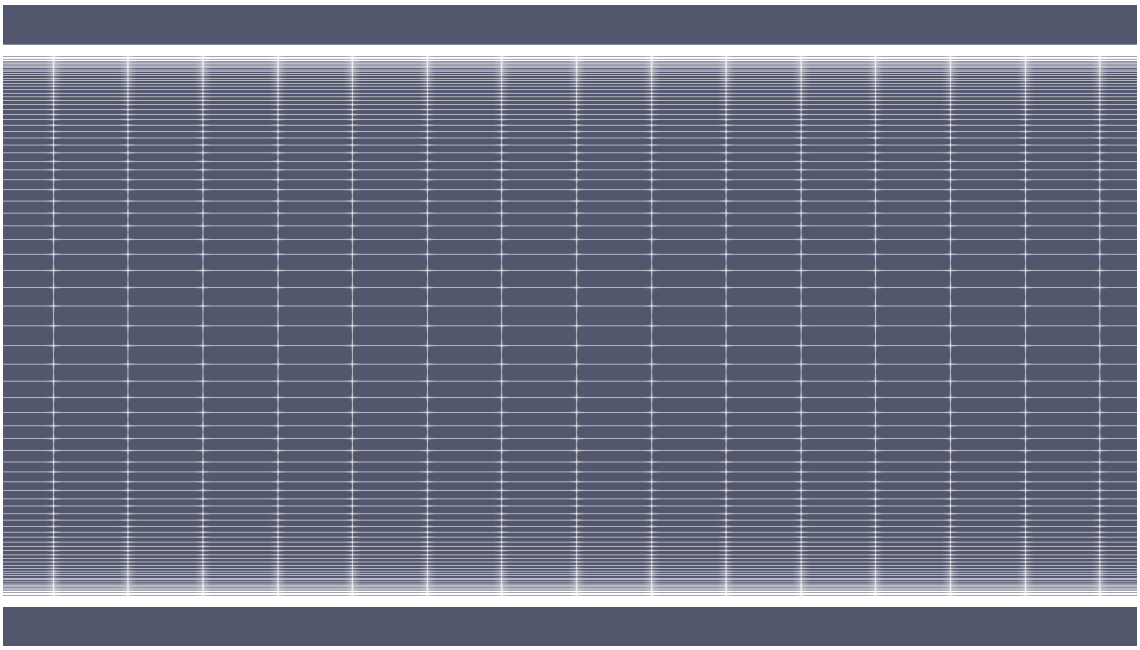

Figure 2.10: Channel Grid

Boundary Conditions

In order to accurately characterize the behaviour of the flow in the rectangular channel, specific boundary conditions have to be implemented. As mentioned before, these boundary conditions are suggested by Masoudian et al..

In order to maintain a consistent flow pattern, a periodic boundary condition is implemented in the stream wise direction. At the top and bottom walls of the channel, no-slip boundary conditions are implemented. For most parameters involved in this study, a value of zero is assigned at the walls, maintaining consistency with physical expectations, with the exception of the parameter C_{kk}, where a zero gradient condition is applied at the wall.

2.5.6 Solver Selection and Numerical Schemes

In order to ensure accurate and precise results, we had to strategically choose a specific solver and numerical scheme. In this research, the SIMPLE algorithm was chosen to solve the coupling between velocity and pressure equations. For discretizing the equations, second-order schemes were employed, balancing computational efficiency with accuracy. The simulations were run with a tolerance of 10^{-6}.

Chapter 3

Theoretical Model Results and Analysis

The following section presents the results obtained from the application of the Theoretical Model Numerical Analysis described in section 2.2. These results are obtained by employing the previously described equations and procedures. We performed a numerical study which resulted in the quantifying of the flow rate out of the inclined water channel. It is important to review section 2.2, for a thorough grasp of the equations and processes used to generate the results given here.

The table below highlights the main fluid properties used in both the theoretical and experimental analyses. These properties, including density, viscosity, and specific gravity, are critical in understanding the fluid's behavior as it moves through the system.

Constant	**Density** $(\rho)\frac{kg}{m^3}$	**Dynamic Viscosity** $(\mu)Pa*s$	**Rest Velocity** $V_1\frac{m}{s}$	**Force of Gravity** (g) $\frac{m}{s}$	**Water Tank Height** (h) m
Value	998	0.001	0	9.81	3.5

Table 3.1: Flow Properties

Following equation 2.2, the velocity of the fluid out of the main tank resulted in:

$$V_{1.2} = 8.29(\frac{m}{s})$$

Variable	K_{Valve}	Force of Gravity (g) $\frac{m}{s}$	V_{valve}
Value	0.05	9.81	8.29

Table 3.2: Valve Head Loss

Following equation 2.3, the head loss due to the ball valve results in:

$$\text{Valve head Loss } h_{valve} = 0.175$$

Variable	Friction Factor (f)	L (m)	D (m)	$V_{pipe}(\frac{m}{s})$
Value	0.0012	0.3	0.3	8.08

Table 3.3: Pipe Head Loss

Following equation 2.4, the head loss due to the pipe results in:

$$\text{Pipe Head Loss } h_{pipe} = 0.0042$$

Variable	K_{elbow}	Force of Gravity (g) $\frac{m}{s}$	V_{elbow}
Value	0.45	9.81	8.07

Table 3.4: Elbow Head Loss

Following equation 2.5, the head loss due to the elbow results in:

$$\text{Elbow Head Loss } h_{elbow} = 1.49$$

Variable	K_{joint}	V_{joint}
Value	0.9	5.98

Table 3.5: Joint Head Loss

Following equation 2.6, the head loss due to the ball socket joint resulted in:

$$\text{Ball Socket Joint Head Loss } h_{joint} = 1.64$$

Variable	$V_{channel}$	Hydraulic Diameter (DH)	Friction Factor (f)	Length of Channel (L)
Value	1.89	0.0146	0.03	4

Table 3.6: Channel Head Loss

Following equation 2.7, the head loss due to the channel resulted in:

$$\text{Channel Head Loss } h_{channel} = 1.50$$

To finalize the Theoretical Model calculations, equation 2.9 was used to compute the exit velocity through the channel at a 12 degree inclination and equation 2.10 was used to compute the channel exit flow rate.

$$\text{Exit Velocity } V_2 = 2.04(\tfrac{m}{s})$$

$$\text{Exit Flow Rate } Q_2 = 33.40GPM$$

Following a similar approach, we adjusted the channel's height to match the new angle of inclination to 11 degrees. Following this change, here are the obtained results.

$$\text{Exit Velocity } V_2 = 1.88(\tfrac{m}{s})$$

$$\text{Exit Flow Rate } Q_2 = 30.94GPM$$

Chapter 4

Experimental Results and Analysis

The following section presents the experimental model's findings, which were obtained using the approach outlined in section 2.4. The process of running the water channel resulted in the experimental flow rate and velocity leaving the channel. The accuracy of the experimental model is supported through the meticulous process of 10 repeated trials for each inclination angle. The obtained results in this section, serve as a validation of the theoretical model and provide insights into the complex interactions and behaviors within the flow system.

Tables 4.1 - 4.4 present the recorded experimental findings for a 12 degree inclination angle of the water channel. The data gathered includes a number of crucial factors, including flow rate, exit velocity, and corresponding weights, each of which illustrates how the fluid behaves under these particular circumstances.

Trial Number	Elapsed Time (s)	Angle	Initial Weight Scale A (lbs)	Final Weight Scale A (lbs)
Experimental Trial 1	30	12	0	77
Experimental Trial 2	60	12	77	145
Experimental Trial 3	90	12	145	213
Experimental Trial 4	120	12	213	286
Experimental Trial 5	150	12	286	355
Experimental Trial 6	180	12	355	419
Experimental Trial 7	210	12	419	480
Experimental Trial 8	240	12	480	540
Experimental Trial 9	270	12	540	600
Experimental Trial 10	300	12	600	655

Table 4.1: Experimental Results Scale A

Trial Number	Elapsed Time (s)	Angle	Initial Weight Scale B (lbs)	Final Weight Scale B (lbs)
Experimental Trial 1	30	12	0	78
Experimental Trial 2	60	12	78	154
Experimental Trial 3	90	12	154	229
Experimental Trial 4	120	12	229	298
Experimental Trial 5	150	12	298	370
Experimental Trial 6	180	12	370	450
Experimental Trial 7	210	12	450	536
Experimental Trial 8	240	12	536	615
Experimental Trial 9	270	12	615	695
Experimental Trial 10	300	12	695	762

Table 4.2: Experimental Results Scale B

Trial Number	Elapsed Time (s)	Angle	Initial Collective Weight (lbs)	Final Collective Weight (lbs)
Experimental Trial 1	30	12	0	155
Experimental Trial 2	60	12	155	299
Experimental Trial 3	90	12	299	442
Experimental Trial 4	120	12	442	584
Experimental Trial 5	150	12	584	725
Experimental Trial 6	180	12	725	869
Experimental Trial 7	210	12	869	1016
Experimental Trial 8	240	12	1016	1155
Experimental Trial 9	270	12	1155	1295
Experimental Trial 10	300	12	1295	1417

Table 4.3: Collective Experimental Results

Trial Number	Collective Weight Change (lbs)	Collective Weight Change (gal)	Flow Rate (GPS)	Flow Rate (GPM)
Experimental Trial 1	155	18.57	0.62	37.15
Experimental Trial 2	144	17.26	0.58	34.51
Experimental Trial 3	143	17.14	0.57	34.27
Experimental Trial 4	142	17.02	0.57	34.03
Experimental Trial 5	141	16.90	0.56	33.79
Experimental Trial 6	144	17.26	0.58	34.51
Experimental Trial 7	147	17.61	0.59	35.23
Experimental Trial 8	139	16.66	0.56	33.31
Experimental Trial 9	140	16.78	0.56	33.55
Experimental Trial 10	122	14.62	0.49	29.24

Table 4.4: Flow Rate Experimental Results

Following the experimental results, the findings were analysed. The steady-state behavior of the fluid inside the channel is depicted by the average flow rate that was determined after 10 trials. The calculated experimental exit velocity provides insight into how the fluid accelerates as it moves through the inclined channel.

$$\textbf{Exit Flow Rate} = 33.96 \text{ GPM}$$

$$\textbf{Exit Velocity} = 2.08 \ \frac{m}{s}$$

Tables 4.5 - 4.8 present the recorded experimental findings for a 11 degree inclination angle of the water channel. The data gathered includes a number of crucial factors, including flow rate, exit velocity, and corresponding weights, each of which illustrates how the fluid behaves under these particular circumstances.

Trial Number	Elapsed Time (s)	Angle	Initial Weight Scale A (lbs)	Final Weight Scale A (lbs)
Experimental Trial 1	30	11	0	61
Experimental Trial 2	60	11	61	132
Experimental Trial 3	90	11	132	176
Experimental Trial 4	120	11	176	242
Experimental Trial 5	150	11	242	309
Experimental Trial 6	180	11	309	368
Experimental Trial 7	210	11	368	429
Experimental Trial 8	240	11	429	499
Experimental Trial 9	270	11	499	550
Experimental Trial 10	300	11	550	605

Table 4.5: Experimental Results Scale A 11 deg

Trial Number	Elapsed Time (s)	Angle	Initial Weight Scale B (lbs)	Final Weight Scale B (lbs)
Experimental Trial 1	30	11	0	65
Experimental Trial 2	60	11	65	120
Experimental Trial 3	90	11	120	196
Experimental Trial 4	120	11	196	259
Experimental Trial 5	150	11	259	333
Experimental Trial 6	180	11	333	405
Experimental Trial 7	210	11	405	480
Experimental Trial 8	240	11	480	559
Experimental Trial 9	270	11	559	628
Experimental Trial 10	300	11	628	690

Table 4.6: Experimental Results Scale B 11 deg

Trial Number	Elapsed Time (s)	Angle	Initial Collective Weight (lbs)	Final Collective Weight (lbs)
Experimental Trial 1	30	11	0	126
Experimental Trial 2	60	11	126	252
Experimental Trial 3	90	11	252	372
Experimental Trial 4	120	11	372	501
Experimental Trial 5	150	11	501	642
Experimental Trial 6	180	11	642	773
Experimental Trial 7	210	11	773	909
Experimental Trial 8	240	11	909	1058
Experimental Trial 9	270	11	1058	1178
Experimental Trial 10	300	11	1178	1295

Table 4.7: Collective Experimental Results 11 deg

Trial Number	Collective Weight Change (lbs)	Collective Weight Change (gal)	Flow Rate (GPS)	Flow Rate (GPM)
Experimental Trial 1	126	15.10	0.50	30.20
Experimental Trial 2	126	15.10	0.50	30.20
Experimental Trial 3	120	14.38	0.48	28.76
Experimental Trial 4	129	15.46	0.52	30.92
Experimental Trial 5	141	16.90	0.56	33.79
Experimental Trial 6	131	15.70	0.52	31.39
Experimental Trial 7	136	16.30	0.54	32.59
Experimental Trial 8	149	17.85	0.60	35.71
Experimental Trial 9	120	14.38	0.48	28.76
Experimental Trial 10	117	14.01	0.47	28.04

Table 4.8: Flow Rate Experimental Results 11 deg

Following the experimental results, the findings were analysed. The steady-state behavior of the fluid inside the channel is depicted by the average flow rate that was determined after 10 trials. The calculated experimental exit velocity provides insight into how the fluid accelerates as it moves through the inclined channel.

$$\textbf{Exit Flow Rate} = 31.04 \text{ GPM}$$

$$\textbf{Exit Velocity} = 1.90 \ \frac{m}{s}$$

Chapter 5

RANS Viscoelastic Turbulence Model Results

5.1 Model Validation

Aiming to validate the accuracy and precision of the turbulence model. Results obtained from the current study were compared to both DNS and RANS data. The initial stage of the model validation revolved around a grid study. Expanding upon the preliminary phase of model validation, a thorough investigation was conducted to evaluate the turbulence model's reliability across various mesh resolutions. Table 2.2, references the three utilized grids, each grid had a different total amount of cells. The purpose of this cell count differentiation was to investigate the responsiveness and flexibility of the turbulence model in relation to various grid structures. During the simulation phase, the viscoelastic Reynolds-Averaged Navier-Stokes (RANS) turbulence model was applied to each of the three grid structures individually. Throughout these simulations, the consistency of parameters and rheological properties was maintained. By maintaining these factors at a constant level, the primary objective was to exclusively analyze any variations or resemblances in the behavior of the turbulence model, solely based on the grid structure. In order to guarantee the objectivity and validity of the simulation outcomes, a comparison was made between the results obtained from each grid structure and a benchmark Direct Numerical Simulation (DNS) solution.

This comparison aimed to identify any deviations in the turbulence model's predictions, as influenced by the grid resolution. The mention grid study analysis can be visually analyzed in figure 5.1 and 5.2.

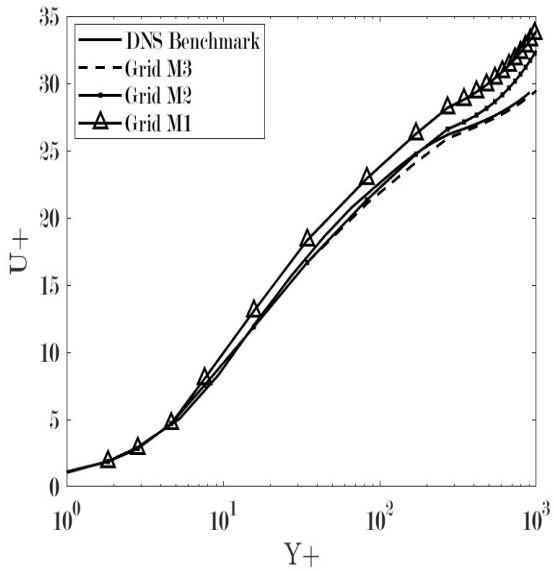

Figure 5.1: Grid Study

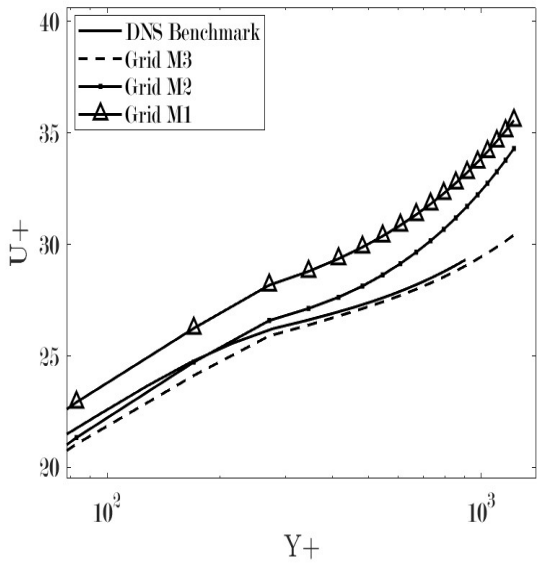

Figure 5.2: Enlarged Grid Study

Both figure 5.1 and 5.2 depict the results of the grid study analysis. The findings of our grid study indicate a significant correlation between the outcomes and the resolution of the grid. In particular, as the grid resolution decreased, the normalized velocity profiles exhibited increasingly pronounced deviations from the benchmark obtained through Direct Numerical Simulation (DNS). The observed deviation was more noticeable in both the log layer and the defect layer. The log layer, which commonly follows the law of the wall, shows a heightened sensitivity to grid resolution due to the interaction between turbulent fluctuations and the mean flow within this region. Similarly, the defect layer, responsible for capturing the deviation of the flow from its free-stream behavior, needs a finely resolved grid in order to precisely capture flow gradients. These findings highlight the significance of grid refinement in turbulence modeling, particularly when aiming for a high level of accuracy.

Following equations 2.39 and 2.40, the percentage of reduced drag was calculated for all three grids and presented in table 5.1.

Grid	N_x*N_y*N_z	$C_{f,vis}$	$C_{f,new}$	DR %
Grid M1	65 x 65 x 1	$9.45 * 10^{-4}$	$1.58 * 10^{-3}$	40.14
Grid M2	111 x 111 x 1	$9.44 * 10^{-4}$	$1.58 * 10^{-3}$	40.20
Grid M3	199 x 199 x 1	$9.42 * 10^{-4}$	$1.58 * 10^{-3}$	40.33

Table 5.1: Drag Reduction Grid Results

These results, corroborate that the refined M3 grid output the best and most accurate results. Table 5.1, reveals that as we refine the mesh, the friction coefficient decreases. This indicates that the wall shear stress also decreases with refinement. Ultimately, drag can be reduced by polymeric solutions in the flow stream.

In their studies, Masoudian et al. and Iaccarino et al. use a constant value of the ratio of solvent viscosity to total viscosity β of 0.9. Aiming to successfully replicate their results

using OpenFOAM software, the value for β remained unchanged. Values for friction Reynolds number (Re_τ), the friction Weissenberg number ($We_{\tau 0}$), and the maximum extension of the polymer chains (L^2) rage widely depending on specific paper. In order to conduct future work using the hydrodynamic lab facilities. The chosen values for friction Reynolds number (Re_τ), the friction Weissenberg number ($We_{\tau 0}$), and the maximum extension of the polymer chains (L^2) were chosen to assimilate as much as possible the flow in the water channel. The chosen grid to compare to historical data and that will continue through this research with the name of "current study" is Grid M3, which showed accuracy and precision. Table 5.2 depict the current study chosen rheological parameters, as well as benchmark DNS and RANS data. These different flow simulations are compared in figure 5.3, which depicts the normalized velocity profile in wall coordinates.

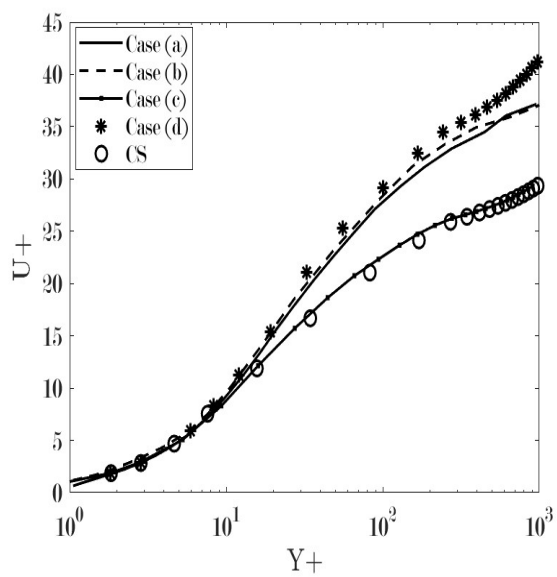

Figure 5.3: Normalized Velocity Profile in Wall Coordinates. Comparison between DNS, RANS and Current Study

As seen in figure 5.3, both DNS data, case (a) and case (b) are fairly similar in the viscous sublayer, the data starts to deviate towards the log and defect layer. This is a direct result

DNS Data	Case	$Re_{\tau 0}$	L^2	$Wi_{\tau 0}$	β
Iaccarino et al.	(a)	300	10,000	120	0.9
Thais et al.	(b)	395	10,000	116	0.9
RANS DATA	Case	$Re_{\tau 0}$	L^2	$Wi_{\tau 0}$	β
Masoudian et al.	(c)	395	100	900	0.9
Masoudian et al.	(d)	396	100	14400	0.9
Current Study	CS	395	100	900	0.9

Table 5.2: Flow Rheological Parameters

of the different values used for the friction Reynolds number (Re_τ), the friction Weissenberg number ($We_{\tau 0}$). Similarly, both RANS data case (c) and (d) deviate starting in the log layer due to the large difference in the friction Weissenberg number ($We_{\tau 0}$).

These profiles show the interactions between viscous forces and inertial effects, especially near boundaries. Presented below in figure 5.4 is a normalized velocity profile, which offers a comparative view of the viscous sublayer, the logarithmic layer, and the Grid M3 solution.

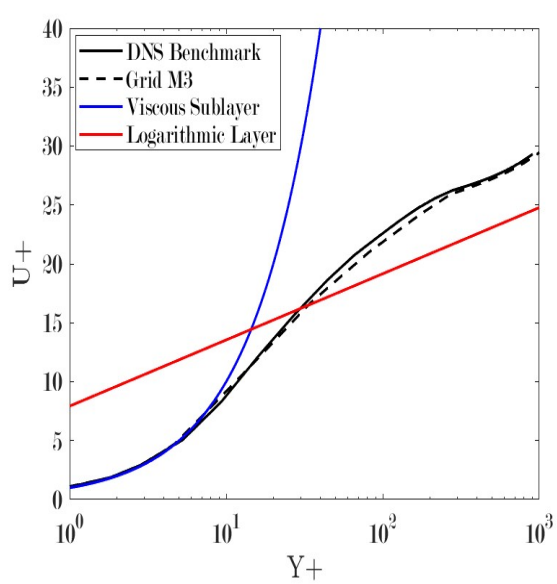

Figure 5.4: Normalized Velocity Profile Law of the Wall Comparison

As appreciated on 5.4, in the region known as the viscous sublayer, where the y+ values

range from 1 to 10, the solution demonstrates a remarkable adherence to the expected linear behavior. This observation highlights the model's ability to effectively represent the near-wall viscous effects with a high degree of accuracy. In the log layer, the solution exhibits a deviation from the expected logarithmic profile known as "law of the wall". The observed phenomenon can is attributed to the presence of polymer additives within the fluid flow. These factors introduce viscoelastic behavior, leading to distinct momentum diffusion characteristics that deviate from those observed in a purely Newtonian turbulent flow. The velocity profile deviations are expected due to the inherent complexities of the viscoelastic Reynolds-Averaged Navier-Stokes (RANS) turbulence model. The proposed solution demonstrates a strong alignment with the theoretical expectations associated with modeling approaches of this nature.

As a final comparison to DNS historical data, the percentage of reduce drag was compared in table 5.3.

Study	$DR\%$	$Re_{\tau 0}$	L^2	$Wi_{\tau 0}$	β
Masoudian et al.	37	395	900	100	0.9
Current Study	40.33	395	900	100	0.9

Table 5.3: Drag Reduction DNS Comparison

As observed in 5.3, the current study exhibited a higher drag reduction than the DNS. The over prediction of the drag reduction is attributed to the fact that the RANS model in our study inherently smooths out certain turbulence structures, leading to an over prediction of drag reduction Masoudian et al.. The over prediction of the drag reduction while important, is minimal. Which makes the viscoelastic RANS turbulence model a viable and reliable cost effective alternative.

5.2 Turbulence Model Comparison

Once our the viscoelastic RANS turbulence model was validated against historical DNS results. The following step was to compare its performance with other established turbulence models under identical geometric conditions. Maintaining consistent computational domains and boundary conditions throughout the simulations ensured that any discrepancies observed were solely attributed to inherent variations in the models.

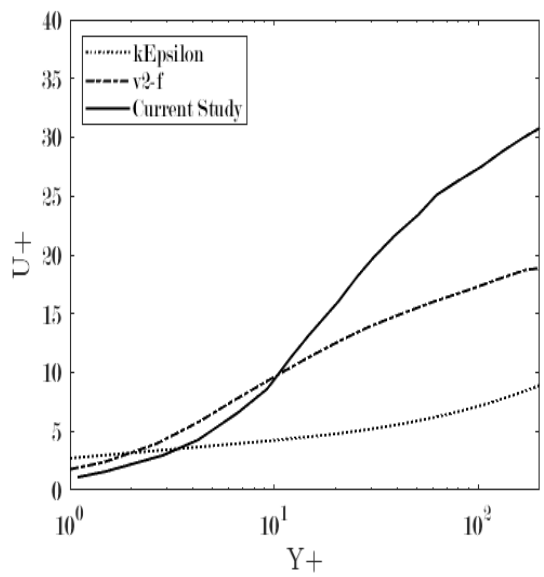

Figure 5.5: Normalized Velocity Profile

Figure 5.5 shows the normalized velocity profile for a k - ϵ turbulence model, a k - ϵ - v^2 - f turbulence model and for the current study's viscoelastic RANS turbulence model. The variations in the $u+$ values observed in the three studies are due to the unique modeling capabilities of each turbulence model and their respective objectives in capturing the underlying physics. The standard k - ϵ model, due to its higher general approach exhibits less precise representation of near-wall effects in comparison to specialized models. The k - ϵ - v^2 - f model, which has been developed to enhance the accuracy of wall region predic-

tions according to Pinho et al., inherently results in higher values of u+ as a result of its improved ability to capture turbulence. The viscoelastic Reynolds-Averaged Navier-Stokes (RANS) model extends its analysis to incorporate the distinct flow resistance exhibited by viscoelastic fluids, resulting in the attainment of the highest $u+$ values.

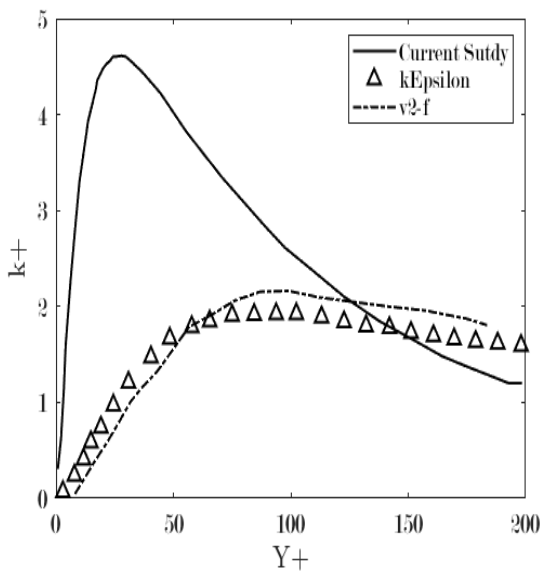

Figure 5.6: Turbulent Kinetic Energy

Figure 5.6, depicts the normalized turbulent kinetic energy, it compares the k - ϵ turbulence model, a k - ϵ - v^2 - f turbulence model and for the current study's viscoelastic RANS turbulence model. The k - ϵ turbulence model, and the k - ϵ - v^2 - f turbulence model align closely, suggesting similar turbulence predictions for the chosen conditions. In contrast, the current study's viscoelastic RANS turbulence model, show a clearly represented peak, which indicates an increased turbulent energy near the wall due to viscoelastic effects. The presence of the mentioned peak in turbulent kinetic energy near the wall impacts the wall shear stresses, the impact on wall shear stress implicates potential for drag reduction as seen in equations 2.39 and 2.40. According to Masoudian et al., this phenomenon has been observed in various viscoelastic systems, where it has been documented to result in drag

reduction. The difference in turbulent kinetic energy appreciated in 5.6 clearly indicates that utilizing conventional models will fail to account for this and other phenomenons resulting in a no accurate solution.

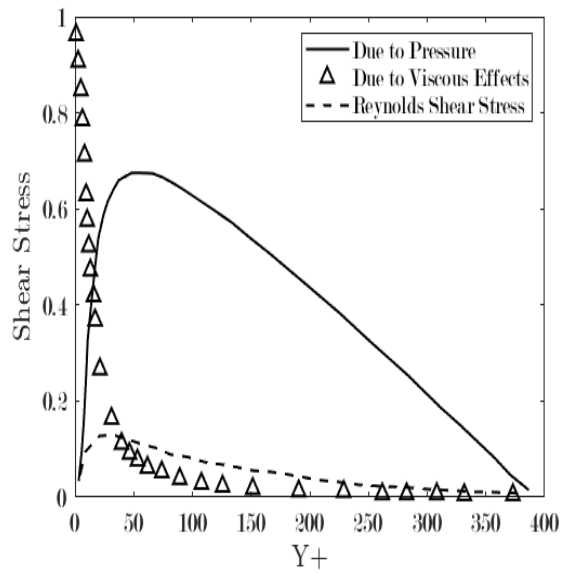

Figure 5.7: Normalized Wall Shear Stress

Figure 5.7, displays the normalized wall shear stress of the current study. The plot shows three main types of shear stress: shear stress due to pressure, due to viscous effects, due to turbulence (Reynolds shear stress). As shown in 5.7, near the walls is where the shear stress are most present. Close to the wall, the shear stress due to viscous effects is dominant. The high shear stress due to viscous effects near the wall is attributed to the sharp velocity gradients Masoudian et al.. Moving away from the wall, the flow becomes less influenced by the wall's no-slip condition, causing the velocity gradient, and thus the viscous shear stress to gradually decrease. The shear stress due to pressure shows a peak near the wall due to significant pressure gradients, often seen in regions where the flow accelerates or decelerates rapidly due to the wall's influence Masoudian et al.. Away from the wall, the flow stabilizes, and pressure variations decrease, leading to a reduction in this shear stress due to pressure

component. Finally, the Reynolds shear stress, has a small increase near the wall due to the interactions between the turbulent eddies and the laminar sublayer Masoudian et al.. Away from the wall the flow becomes more homogeneous resulting in a decrease in Reynolds shear stress.

Figure 5.7, provides an in depth description of the various shear stress components present in the current study's viscoelastic flow. The explanation regarding the near wall behaviour provides insight and understanding on the flow's physics. This understanding is crucial for accurate flow predictions and optimization.

5.3 Solvent Viscosity to Polymer Viscosity Ratio (β) Analysis

The ratio of solvent viscosity to polymer viscosity (β) is one a crucial factors that affects drag reduction. This ratio represents the intricate relationship between a polymer's flow resistance and the solvent Brostow. It is of interest for this study, due to the multiple types of polymers in the Hydrodynamics Lab. The ratio comes from the choice of the polymer. Different polymers, based on their molecular weight, and structure have distinct viscosities when dissolved. The combination between the solvent and polymer viscosity can drastically affect the drag reduction capabilities of the resulting solution Brostow. The purpose of this section is to fully evaluate the sensitivity of the model proposed by Masoudian et al. for different polymers which translates into the solvent to polymer viscosity ratios (β).

As shown in figure 5.4 and in table 5.3, at high solvent to polymer viscosity ratios ($\beta = 0.9$), the viscoealstic RANS turbulence model matches its DNS benchmark almost perfectly. Figure 5.8, provides a DNS comparison at a lower solvent viscosity to polymer viscosity ratio (β).

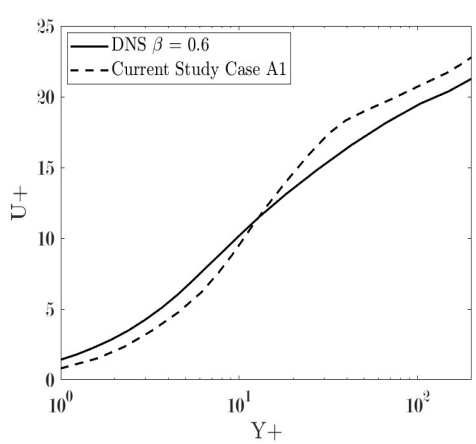

Figure 5.8: Low β DNS Comparison

As shown on figure 5.8, as the solvent viscosity to polymer viscosity ratio is decreased, the results from the simulation start to diverge from the DNS benchmark. To further analyze this discrepancy. We performed simulations with an even lower Solvent Viscosity to Polymer Viscosity Ratio. The goal of this was to find any recurring patterns as the solvent viscosity to polymer viscosity ratio dropped. This analysis will make it clear how this parameter affects the model.

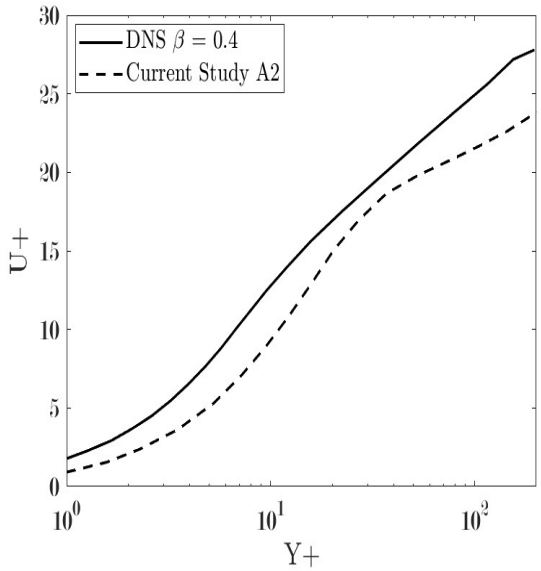

Figure 5.9: Low β DNS Comparison

As anticipated, 5.9 demonstrates that as the solvent viscosity to polymer viscosity ratio decrease even further, the alignment of the solution with the DNS benchmark diverges even further. After observing these discrepancies, we computed the percentage of drag reduction to further assess the impact of the solvent viscosity to polymer viscosity ratio on flow efficiency. Table 5.4, displays a comparison between the DNS benchmarks and the computed percent of drag reduced.

Study	β	DR%
Li et al. DNS Data	0.6	26
Current Study A1	0.6	30
Li et al. DNS Data	0.4	64
Current Study A2	0.4	12

Table 5.4: Solvent Viscosity to Polymer Viscosity Ratio (β) DNS Comparison

As observed in this section, the viscoelastic RANS turbulence model developed by Masoudian et al. shows a decline in performance and accuracy at lower solvent viscosity to polymer viscosity ratios. This observation highlights that the the viscoelastic RANS turbulence model developed by Masoudian et al. can successfully reproduce DNS results at higher solvent viscosity to polymer viscosity ratios, it struggles to maintain its accuracy and predictive capability at lower solvent viscosity to polymer viscosity ratios.

Chapter 6

Conclusions & Future Work

In the present study we deeply comprehended the fundamental principles of fluid dynamics, performed both theoretical and experimental analyses of the hydrodynamic laboratory in Virginia Tech, and evaluated the viscoelastic RANS turbulence model developed by Masoudian et al. in predicting Drag Reduction (DR) values. In order to do so; a theoretical model was developed to predict the flow rate out of the inclined channel. An empirical approach was taken in order to compute the experimental flow rate out of the inclined channel in the Hydrodynamics Lab. Finally, we conducted an extensive evaluation of the viscoelastic RANS turbulence model. These approaches revealed the following.

1. The developed theoretical model employed to predict the flow rate out of the inclined channel in the Hydrodynamics Lab predicted that for an inclination of 12 degrees. The predicted exit velocity and exit flow rate out of the inclined chanel are 2.04 $\frac{m}{s}$ and 33.40 GPM respectively. The same approach but for an 11 degree inclination predicted a 1.88 $\frac{m}{s}$ exit velocity, and a 30.94 GPM volumetric flow rate.

2. The empirical approach taken in order to compute the experimental flow rate out of the inclined channel in the Hydrodynamics Lab demonstrated that for an inclination of 12 degrees. The experimental exit velocity and exit flow rate out of the inclined channel are 2.08 $\frac{m}{s}$ and 33.96 GPM. The same approach but for an 11 degree inclination demonstrated an exit velocity of 1.90 $\frac{m}{s}$ and a 31.04 GPM volumetric flow rate.

3. The analysis and evaluation of the viscoelastic RANS turbulence model developed by Masoudian et al. showed that:

   (a) The viscoelastic RANS turbulence model developed by Masoudian et al. shows a high accuracy in percent of drag reduced, velocity and wall shear stress profiles when compared to DNS historical data at higher solvent viscosity to polymer viscosity ratios.

   (b) The viscoelastic RANS turbulence model developed by Masoudian et al. shows a clear difference in velocity and wall shear stress profiles to the k - ϵ and k - $\epsilon - v^2 - f$ turbulence models. This proves that the utilization of the mentioned turbulence models when modeling viscoelastic flows will result in a non accurate solution.

   (c) In lower solvent viscosity to polymer viscosity ratios, the viscoelastic RANS turbulence model developed by Masoudian et al. could not predict accurate percentages of drag reduced, and was not able to follow DNS benchmark normalized velocity profile results.

6.1 Recommendations for Future Work

The research conducted has revealed significant findings and identified opportunities where further investigation can be done. In this section, we analyze the areas of opportunity where further actions can be undertaken. Our objective is to provide guidance for future research endeavors in this field by addressing emerging challenges and further developing our existing knowledge. There are several key areas that present themselves as promising subjects for further investigation in order to enhance our comprehension and improve our methodologies

1. **Experimental Setup** The primary focus on the experimental front, should be to fully install the necessary hardware to ensure that the hydrodynamics laboratory water channel is able to successfully operate while a polymeric solution is being injected. To do so, new injector slots should be installed and a pumping mechanism has to be designed in order to ensure proper polymer injection tangential to the to the flow at a pre calculated injection flow rate.

2. **Model Verification** Once the experimental model has been tested strictly for higher solvent viscosity to polymer viscosity ratios, validating these results with the viscoelastic RANS turbulence model developed by Masoudian et al. becomes essential. The predictive accuracy of this model will be confirmed by the successful replication of experimental data through it.

3. **Model Refinement** As stated in the current research, the viscoelastic RANS turbulence model developed by Masoudian et al. is not accurate in replicating result for simulations with lower solvent viscosity to polymer viscosity ratios. A rigorous effort should be dedicated to enhancing the viscoelastic RANS turbulence model developed by Masoudian et al.. The aim is to fine tune its capabilities to accurately represent flows at any solvent to polymer viscosity ratios.

4. **Drag Reduction Optimization** Having both the improved experimental water channel and the optimized viscoelastic RANS turbulence model which now have been proven to predict the Drag Reduction accurately at any solvent viscosity to polymer viscosity ratio. An exhaustive analysis must be conducted to determine the optimal polymer type and concentration that yield the most favorable outcomes in terms of flow characteristics.

5. **Industry Application Assessment** The culmination of the future work would require a a comprehensive analysis to determine the ideal polymer and solvent mix for the most effective drag reduction. The goal would be to obtain the perfect combination that not only maximizes drag reduction, but also in ensures minimal weight addition when loaded onto vessels. The objective would be to achieve a balance in which the benefits of drag reduction are obtained without adding to much extra weight from the polymer solution.

The mentioned steps serve as a clear plan of action for our drag reduction research. Our strategy prioritizes both accuracy and applicability and aims to address current issues while laying a solid foundation for future research. This approach makes sure that the work we conduct in this area is both valuable and scalable for later research.

Bibliography

[1] Agarwal, A., Brandt, L., and Zaki, T. A. (2015). Transition to turbulence in viscoelastic channel flow. *Procedia IUTAM*, 14:519–526.

[2] Azad, S., Riasi, A., Darian, H. M., and Moghadam, H. A. (2017). Parametric study of a viscoelastic rans turbulence model in the fully developed channel flow. *Applied and Computational Mechanics*, 48:65–74.

[3] Batchelor, G. K. (1967). *An introduction to fluid dynamics*. Cambridge university press.

[4] Bird, R. B. and Armstrong, R. (1987). 0. hassager, dynamics of polymeric liquids. *Fluid Mechanics*, 1.

[5] Brostow, W. (2008). Drag reduction in flow: Review of applications, mechanism and prediction. *Journal of industrial and Engineering Chemistry*, 14(4):409–416.

[6] De Gennes, P.-G. (1990). *Introduction to polymer dynamics*. CUP Archive.

[7] Dimitropoulos, C. D., Dubief, Y., Shaqfeh, E. S., Moin, P., and Lele, S. K. (2005). Direct numerical simulation of polymer-induced drag reduction in turbulent boundary layer flow. *Physics of Fluids*, 17(1).

[8] Dimitropoulos, C. D., Sureshkumar, R., and Beris, A. N. (1998). Direct numerical simulation of viscoelastic turbulent channel flow exhibiting drag reduction: effect of the variation of rheological parameters. *Journal of Non-Newtonian Fluid Mechanics*, 79(2-3):433–468.

[9] D'Alessio, S. (2021). Torricelli's law revisited. *European Journal of Physics*, 42(6):065808.

[10] Fox, R. W., RW, P., and PJ, M. A. (2011). Introduction to fluid mechanics, octave. ed.

[11] Hoyt, J. (1972). A freeman scholar lecture: The effect of additives on fluid friction.

[12] Iaccarino, G., Shaqfeh, E. S., and Dubief, Y. (2010). Reynolds-averaged modeling of polymer drag reduction in turbulent flows. *Journal of Non-Newtonian Fluid Mechanics*, 165(7-8):376–384.

[13] Idelchik, I. E. (1986). Handbook of hydraulic resistance. *Washington*.

[14] Jasak, H. (2009). Openfoam: Open source cfd in research and industry. *International Journal of Naval Architecture and Ocean Engineering*, 1(2):89–94.

[15] Kalelkar, C., Govindarajan, R., and Pandit, R. (2005). Drag reduction by polymer additives in decaying turbulence. *Physical Review E*, 72(1):017301.

[16] Khambhampati, K. T. and Handler, R. A. (2020). Numerical simulation of the swirling flow of a finitely extensible non-linear elastic peterlin fluid. *Physics of Fluids*, 32(10).

[17] Li, C.-F., Sureshkumar, R., and Khomami, B. (2006). Influence of rheological parameters on polymer induced turbulent drag reduction. *Journal of Non-Newtonian Fluid Mechanics*, 140(1-3):23–40.

[18] Lumley, J. L. (1973). Drag reduction in turbulent flow by polymer additives. *Journal of Polymer Science: Macromolecular Reviews*, 7(1):263–290.

[19] Masoudian, M., Kim, K., Pinho, F., and Sureshkumar, R. (2013). A viscoelastic k-ε-v2-f turbulent flow model valid up to the maximum drag reduction limit. *Journal of Non-Newtonian Fluid Mechanics*, 202:99–111.

[20] McComb, W. and Rabie, L. (1982). Local drag reduction due to injection of polymer solutions into turbulent flow in a pipe. part i: Dependence on local polymer concentration. *AIChE Journal*, 28(4):547–557.

[21] Min, T., Yoo, J. Y., Choi, H., and Joseph, D. D. (2003). Drag reduction by polymer additives in a turbulent channel flow. *Journal of Fluid Mechanics*, 486:213–238.

[22] Moody, L. F. (1944). Friction factors for pipe flow. *Transactions of the American Society of Mechanical Engineers*, 66(8):671–678.

[23] Munson, B. R., Young, D. F., Okiishi, T. H., and Huebsch, W. W. (2006). Fundamentals of fluid mechanics, john wiley & sons. *Inc., USA*.

[24] Pinho, F. (2003). A gnf framework for turbulent flow models of drag reducing fluids and proposal for ak–ε type closure. *Journal of Non-Newtonian Fluid Mechanics*, 114(2-3):149–184.

[25] Pinho, F., Li, C., Younis, B., and Sureshkumar, R. (2008). A low reynolds number turbulence closure for viscoelastic fluids. *Journal of Non-Newtonian Fluid Mechanics*, 154(2-3):89–108.

[26] Pope, S. B. (2000). *Turbulent flows*. Cambridge university press.

[27] Ptasinski, P., Boersma, B., Nieuwstadt, F., Hulsen, M., Van den Brule, B., and Hunt, J. (2003). Turbulent channel flow near maximum drag reduction: simulations, experiments and mechanisms. *Journal of Fluid Mechanics*, 490:251–291.

[28] Ptasinski, P., Nieuwstadt, F., Van Den Brule, B., and Hulsen, M. (2001). Experiments in turbulent pipe flow with polymer additives at maximum drag reduction. *Flow, Turbulence and Combustion*, 66:159–182.

[29] Sureshkumar, R., Beris, A. N., and Handler, R. A. (1997). Direct numerical simulation of the turbulent channel flow of a polymer solution. *Physics of Fluids*, 9(3):743–755.

[30] Thais, L., Gatski, T. B., and Mompean, G. (2012). Some dynamical features of the turbulent flow of a viscoelastic fluid for reduced drag. *Journal of Turbulence*, (13):N19.

[31] Toms, B. A. (1949). Some observations on the flow of linear polymer solutions through straight tubes at large reynolds numbers. *Proc. First Int. Conger. on Rheology*, 2:135–141.

[32] Van Der Meulen, J. (1974). Friction reduction and degradation in turbulent flow of dilute polymer solutions. *Applied Scientific Research*, 29:161–174.

[33] Virk, P. S. (1975). Drag reduction fundamentals. *AIChE Journal*, 21(4):625–656.

[34] Walker, D., Tiederman, W., and Luchik, T. (1986). Optimization of the injection process for drag-reducing additives. *Experiments in fluids*, 4(2):114–120.

[35] Warholic, M., Massah, H., and Hanratty, T. (1999). Influence of drag-reducing polymers on turbulence: effects of reynolds number, concentration and mixing. *Experiments in fluids*, 27(5):461–472.

[36] White, C. M. and Mungal, M. G. (2008). Mechanics and prediction of turbulent drag reduction with polymer additives. *Annu. Rev. Fluid Mech.*, 40:235–256.

[37] White, F. M. (1994). Fluid mechanics, mcgraw-hill. *New York*.

[38] White, F. M. and Majdalani, J. (2006). *Viscous fluid flow*, volume 3. McGraw-Hill New York.

[39] Wu, J., Fruman, D., and Tulin, M. (1978). Drag reduction by polymer diffusion at high reynolds numbers. *Journal of Hydronautics*, 12(3):134–136.

[40] Wu, J. and Tulin, M. P. (1972). Drag reduction by ejecting additive solutions into pure-water boundary layer.